AD/A-010 627

ATMOSPHERIC MODELING: DEVELOPMENT OF VORTEX STRUCTURES IN BUOYANT AND SHEAR FLOWS

J. ALEX THOMSON, ET AL
PHYSICAL DYNAMICS, INCORPORATED

PREPARED FOR:

ROME AIR DEVELOPMENT CENTER DEFENSE ADVANCED RESEARCH PROJECTS AGENCY DECEMBER 1973

DISTRIBUTED BY:



RADC-TR-74-117 Final Technical Report December 1973



ATMOSPHERIC MODELING: DEVELOPMENT OF VORTEX STRUCTURES IN BUOYANT AND SHEAR FLOWS

Physical Dynamics, Incorporated

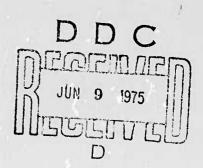
Sponsored By
Defense Advanced Research Projects Agency
ARPA Order No. 1649

Approved for public release; distribution unlimited.

The views and conclusions contained in this document are those of the authors and should not be interpreted as necessarily representing the official policies, either expressed or implied, of the Defense Advanced Research Projects Agency or the U. S. Government.

Rome Air Development Center Air Force Systems Command Griffiss Air Force Base, New York

Reproduced by
NATIONAL TECHNICAL
INFORMATION SERVICE
U S Department of Commerce
Springfield VA 22151



SECURITY CLASSIFICATION OF THIS PAGE (When Data Entered)

The state of the s	AGE	READ INSTRUCTIONS BEFORE COMPLETING FORM
REPORT NUMBER	GOVT ACCESSION NO.	3. RECIPIENT'S CATALOG NUMBER
RADC-TR-74-117		
TITLE (and Subtitle)		5. TYPE OF REPORT & PERIOD COVERED
Atmospheric Modeling: Development of		
Vortex Structures in Buoyant	and Shear	Final Report(1 Aug 72-1
Flows		6. PERFORMING ORG. REPORT NUMBER PD-73-034
AUTHOR(s)		8. CONTRACT OR GRANT NUMBER(s)
J. Alex Thomson		
J. C. S. Meng		F30602-72-C-0493
PERFORMING ORGANIZATION NAME AND ADDRESS		
	V 1 1 2	10. PROGRAM ELEMENT, PROJECT, TASK AREA & WORK UNIT NUMBERS
Physical Dynamics, Inc. P.O. Box 604		62301D
College Park Station		16490403
Detroit, MI 48221 CONTROLLING OFFICE NAME AND ADDRESS		12. REPORT DATE
Defense Advanced Research Pro	jects Agency	Dec 1973
1400 Wilson Blvd		13. NUMBER OF PAGES
Arlington, VA 22209		143
MONITORING AGENCY NAME & ADDRESS(If different	from Controlling Office)	1S. SECURITY CLASS. (of this report)
RADC/OCSE		
ATTN: L. Strauss Griffiss AFB, NY 13441		Uncl.
GITTISS AID, NI 15441		15a. DECLASSIFICATION DOWNGRADING SCHEDULE
7. DISTRIBUTION STATEMENT (of the abstract entered in	n Block 20, if different fro.	m Report)
11	n Block 20, il dillerent Iro.	m Report)
11	n Block 20, If different fro.	m Report)
11	n Block 20, il dillerent Iro.	m Report)
S. SUPPLEMENTARY NOTES The KEY WORDS (Continue on reverse side if necessary and	I identily by block number)	
SUPPLEMENTARY NOTES KEY WORDS (Continue on reverse side if necessary and atmospheric modeling fast	Identilly by block number) fourier tran	nsform
S. SUPPLEMENTARY NOTES KEY WORDS (Continue on reverse side if necessary and atmospheric modeling fast vorticity nume	I identily by block number)	nsform
S. SUPPLEMENTARY NOTES KEY WORDS (Continue on reverse side if necessary and atmospheric modeling fast vorticity nume finite differences	Identilly by block number) fourier tran	nsform
S. SUPPLEMENTARY NOTES KEY WORDS (Continue on reverse side if necessary and atmospheric modeling fast vorticity nume	Identilly by block number) fourier tran	nsform
S. SUPPLEMENTARY NOTES S. KEY WORDS (Continue on reverse side if necessary and atmospheric modeling fast vorticity nume finite differences instability D. ABSTRACT (Continue on reverse side if necessary and The first particle-in-center)	Identify by block number) fourier transcrical calculations of the control of the	nsform ations
8. SUPPLEMENTARY NOTES S. KEY WORDS (Continue on reverse side if necessary and atmospheric modeling fast vorticity nume finite differences instability S. ABSTRACT (Continue on reverse side if necessary and The first particle-in-cathe vortex by the particles was	identify by block number) fourier transcrical calcula dentify by block number) cell (PIC) cal as, to the aut	asform ations lculation representing thors' knowledge, done b
E. SUPPLEMENTARY NOTES S. KEY WORDS (Continue on reverse side if necessary and atmospheric modeling fast vorticity nume finite differences instability D. ABSTRACT (Continue on reverse side if necessary and The first particle-in-cathe vortex by the particles was cosenhead in 1930 in his study	Identify by block number) fourier transcrical calcula Identify by block number) cell (PIC) cal as, to the aut of vortex st	sform ations culation representing thors' knowledge, done b
REY WORDS (Continue on reverse side if necessary and atmospheric modeling fast vorticity nume finite differences instability D. ABSTRACT (Continue on reverse side if necessary and number first particle-in-continue on reverse side if necessary and the vortex by the particles was cosenhead in 1930 in his study nation was repeated by Birkhof	Identify by block number) fourier transcrical calcula identify by block number) cell (PIC) calculated to the autor of vortex standers	sform ations lculation representing thors' knowledge, done b treets. The same calcu- in 1959 and by Hama and
S. SUPPLEMENTARY NOTES R. KEY WORDS (Continue on reverse side if necessary and atmospheric modeling fast vorticity nume finite differences instability R. ABSTRACT (Continue on reverse side if necessary and the first particle—in—content to the vortex by the particles was cosenhead in 1930 in his study ation was repeated by Birkhof Burke in 1960. Abernathy and	Identify by block number) fourier transcrical calcula identify by block number) cell (PIC) calculated to the autor of vortex stand Fisher Kronauer made	asform ations lculation representing thors' knowledge, done b treets. The same calcu- in 1959 and by Hama and e a detailed study of
S. SUPPLEMENTARY NOTES REY WORDS (Continue on reverse side if necessary and atmospheric modeling fast vorticity nume finite differences instability RESTRACT (Continue on reverse side if necessary and the vortex by the particle-in-center of the vortex by the particles was cosenhead in 1930 in his study ation was repeated by Birkhof	Identify by block number) fourier transcrical calculations, to the autor of vortex stand Fisher Kronauer made 162 using the	asform ations lculation representing thors' knowledge, done be treets. The same calcu- in 1959 and by Hama and e a detailed study of same method. Hockney

Fourier transform (FFT) to the PIC method in order to handle very

UNERICES ISTRAFECT TO CHANGE

SECURITY CLASSIFICATION OF THIS PAGE(When Data Entered)

large numbers of particles, usually in the order of 10⁵ in the galaxy simulations. Chorin (1973) proposed a new version of the discrete vortex method where vortices are needed only to satsify the no-slip boundary conditions. Along these lines, due to the natural stratification of the atmosphere and the existence of wind shear, almost all atmospheric flows are rotational as a result of the interaction between shear and buoyancy. The numerical study presented herein combines the concepts of the PIC method, Green's function and the FFT methods and may be dubbed the vortex-in-cell (VIC) method.

ATMOSPHERIC MODELING: DEVELOPMENT OF VORTEX STRUCTURES IN BUOYANT AND SHEAR FLOWS

J. Alex Thomson J. C. S. Meng

Contractor: Physical Dynamics, Incorporated Contract Number: F30602-72-C-0493
Effective Date of Contract: 1 August 1972
Contract Expiration Date: 31 December 1973
Amount of Contract: \$50,796.00
Program Code Number: 2E20

Principal Investigator: J. Alex Thomson Phone: 415 848-3063

Contract Engineer: Leonard Strauss
Phone: 315 330-3055

Approved for public release; distribution unlimited.

This research was supported by the Defense Advanced Research Projects Agency of the Department of Defense and was monitored by Leonard Strauss, RADC (OCSE), GAFB, NY 13441 under Contract F30602-72-C-0493.



PUBLICATION REVIEW

This technical report has been reviewed and is approved.

RADC Project Engineer

ABSTRACT

The first particle-in-cell (PIC) calculation representing the vortex by the particles was, to the authors' knowledge, done by Rosenhead in 1930 in his study of vortex streets. The same calculation was repeated by Birkhoff and Fisher in 1959 and by Hama and Burke in 1960. Abernathy and Kronauer made a detailed study of the Karman vortex street in 1962 using the same method. Hockney (1962) was the first one to incorporate the advantages of the fast Fourier transform (FFT) to the PIC method in order to handle very large numbers of particles, usually in the order of 10⁵ in the galaxy simulations. Chorin (1973) proposed a new version of the discrete vortex method where vortices are needed only to satisfy the no-slip boundary conditions. Along these lines, due to the natural stratification of the atmosphere and the existence of wind shear, almost all atmospheric flows are rotational as a result of the interaction between shear and buoyancy. The numerical study presented herein combines the concepts of the PIC method, Green's function and the FFT methods and may be dubbed the vortex-in-cell (VIC) method.

The discrete vortices are treated as the marker particles on an Eulerian grid with the velocity field solved from the updated vorticity distribution. The velocity field can

either be calculated from the distribution of the vortices by Green's function formalism or by the FFT. The computation time required for Green's function formalism is proportional to the square of the number of the vortices N2, while that of the FFT is fixed to $M_{x}^{M}_{y}$ in $(M_{x}^{M}_{y})$, where M_{x}^{M}, M_{y} are the number of mesh points in the x and y directions. Therefore, the FFT formalism can deal with a problem of a very large number of particles without increasing the computation time. The VIC method can also simulate the physical process exactly through which the flow containing or generating vorticity evolves. If it is clear that the essence of turbulence is vortex interactions and decays, then certainly a method directly dealing with such motion should be a valid simulation of the turbulence. The inclusion of the viscosity using Chorin's (1973) method, and generalization to threedimensional formalism, will further extend the range of the relevance to turbulence. The basic economy saved by the VIC method is not only due to the efficient numerical aspects of the schemes but also is due to the basic idea that the flow is dominated by the rotational motion generated by the discretized vortices, and it is wasteful to compute the passive portion of the flow which stays passive and irrotational.

Various problems in different applications have been solved by this method; these are:

Meteorology Kelvin-Helmholtz wave generation

Oceanography Collapsing wakes at ocean thermocline

Buoyant wakes near an ocean thermocline

Aerodynamics Karman vortex street

Aircraft trailing vortex in a wind

shear field

A thermal

An injection cylinder

Flow in porous medium

A study of interfacial finger-like

flow structures.

Good agreement with experiments was obtained.

TABLE OF CONTENTS

			page
ABSTR	ACT		iii
LIST	OF FIGU	RES	vii
I.	INTROD	UCTION	1
II.	FORMUL	ATION: OF THE PROBLEM	7
	II.1	General	7
	II.2	Inviscid Fluids	9
	II.3	Porous Medium or Viscous Flows	11
	II.4	The Case of Large Density Differences	13
	II.5	Vorticity Equations with Surface Tension Effects	16
III.	SCALIN	G AND LABORATORY SIMULATION	22
	III.1	Rise of an Injection Cylinder	23
	III.2	Rise of a Buoyant Cylinder (Thermal)	27
	III.3	Finite Amplitude Kelvin-Helmholtz Waves	52
	III.4	Development of the Kármán Vortex Street	65
	III.5	Aircraft Trailing Vortex Street	76
	III.6	Collapsing Wake on an Ocean Thermocline	89
	III.7	Buoyant Wake Near an Ocean Thermocline	99
	III.8	Saffman-Taylor Instability	112
REFE	RENCES		128

LIST OF FIGURES

Figure		Page
1.1	Initial Vortex Position of an Injection Cylinder	28
1.2	Injection Cylinder at $\tau = .2$	29
1.3	Injection Cylinder at $\tau = .4$	30
1.4	Vortex Pair Developed from an Injection Cylinder	31
2.1	Initial Vortex Position of a Buoyant Cylinder	38
2.2	A Buoyant Cylinder at $\tau = .4$	39
2.3	A Buoyant Cylinder at $\tau = .72$	40
2.4	Vortex Pair Developed from a Buoyant Cylinder at τ = 1	41
2.5	Vortex Pair Developed for a Buoyant Cylinder at $\tau = 1.56$	42
2.6	The Width and Height of the Vortex Pair vs. Time	43
2.7a	Initial Vortex Position of a Buoyant Cylinder	44
2.7b	Velocity Vector Plot of the Initial Vortex Position	45
2.3a	A Buoyant Cylinder at $\tau = .72$	46
2.8b	Velocity Vector Plot of a Buoyant Cylinder at $\tau = .72$	47
2.9	Vortex Pair Developed from a Buoyant Cylinder at τ = 1	48
2.10	Vortex Pair Developed from a Buoyant Cylinder at τ = 1.56	49
2.11a	Vortex Pair Developed from a Buoyant Cylinder at τ = 1.96	50
2.11b	Velocity Vector Plot of a Vortex Pair at $\tau = 1.96$	51
3.1	Initial Disturbance on a Vortex Sheet	55
3.2	Kelvin-Helmholtz Wave in Pure Shear Case at $\tau = .64$	56
3.3	Kelvin-Helmholtz Wave in Pure Shear Case at $\tau = 1.04$	57

List of Figures - Continued

Figure		Page
3.4	Kelvin-Helmholtz Wave in Pure Shear Case at $\tau = 2$	58
3.5	Initial Disturbance in a Vortex Street in an U nstably-Stratified Medium	59
3.6	Kelvin-Helmholtz Wave in Unstable Case at $\tau = .57$	60
3.7	Kelvin-Helmholtz Wave in Unstable Case at $\tau = .81$	61
3.8	Kelvin-Helmholtz Wave in Unstable Case at $\tau = 2$	62
3.9	Kelvin-Helmholtz Wave in a Stably Stratified Medium at $\tau = .99$	63
3.10	Kelvin-Helmholtz Wave in Stable Case at $\tau = 2.01$	64
4.1	Initial Disturbance ($h/\lambda = .28$) on a Pair of Vortex Street	68
4.2	Development of a Vortex Street for $h/\lambda = .28$ at $\tau = .62$	69
4.3	Development of Vortex Street for $h/\lambda = .28$ at $\tau = 1.2$	70
4.4	Distribution of Vortices in a Kármán Vortex Street	71
4.5	Initial Disturbance $n/\lambda = .12$ on a Pair of Vortex Street	72
4.6	Development of Vortex Street for $h/\lambda = .12$ at $\tau = .92$	73
4.7	Development of Vortex Street for $h/\lambda = .12$ at $\tau = 1.5$	74
4.8	Development of Vortex Street for $h/\lambda = .12$ at $\tau = 2.14$	75
5.1	Determination of the Strength of the Aircraft Trailing Vortex	82
5.2a	Initial Aircraft Trailing Vortex Configuration	83
5.2b	Initial Aircraft Trailing Vortex Configuration	84
5.3	Aircraft Trailing Vortex Configuration at T = 2.08 seconds	85

List of Figures - Continued

Figure		Page
5.4	Aircraft Trailing Vortex Configuration at T = 4.08 Seconds	86
5.5a	Aircraft Trailing Vortex Configuration at T = 10 Seconds	87
5.5b	Aircraft Trailing Vortex Configuration at T = 10 Seconds	. 88
6.la	Initial Geometry of a Cylindrical Wake at Ocean Thermocline	91
6.1b	Initial Geometry of a Cylinderical Wake at Ocean Thermocline	92
6.2a	Collapsing Wake on an Ocean Thermocline at $\tau = .6$	93
6.2b	Collapsing Wake on an Ocean Thermocline at $\tau = .6$	94
6.3a	Collapsing Wake on an Ocean Thermocline at $\tau = 1.6$	95
6.3b	Collapsing Wake on an Ocean Thermocline at $\tau = 1.6$	96
6.4a .	Collapsing Wake on Ocean Thermocline at $\tau = 2.2$	97
6.4b	Collapsing Wake on Ocean Thermocline at $\tau = 2.2$	98
7.la	Buoyant Wake Near an Ocean Thermocline	102
7.1b	Buoyant Wake Near an Ocean Thermocline	103
7.2a	Buoyant Wake Near an Ocean Thermocline at $\tau = .6$	104
7.2b	Buoyant Wake Near an Ocean Thermocline at $\tau = .6$	105
7.3a	Buoyant Wake Near an Ocean Thermocline at $\tau = 1.38$	106
7.3b	Buoyant Wake Near an Ocean Thermocline at $\tau = 1.38$	107
7.4a	Buoyant Wake Near an Ocean Thermocline at $\tau = 1.89$	108
7.4b	Buoyant Wake Near an Ocean Thermocline at $\tau = 1.89$	109

List of Figures - Continued

Figure		Page
7.5a	Buoyant Wake Near an Ocean Thermocline at $\tau = 3.00$	110
7.5b	Buoyant Wake Near an Ocean Thermocline at $\tau = 3.00$	111
8.1	Development of Finger-Like Structure in Porous Medium	118
8.2	Initial Disturbance for the Saffman-Taylor Instability Study	119
8.3	Saffman-Taylor Instability Study at $\tau = .22$	120
8.4	Saffman-Taylor Instability Study at $\tau = .38$	121
8.5	Saffman-Taylor Instability Study at $\tau = .46$	122
8.6	Saffman-Taylor Instability Study at τ = .98	123
8.7	Saffman-Taylor Instability Study at $\tau = .22$	124
8.8	Saffman-Taylor Instability Study at $\tau = .38$	125
8.9	Saffman-Taylor Instability Study at $\tau = .46$	126
8.10	Saffman-Taylor Instability Study at $\tau = .98$	127

DEVELOPMENT OF VORTEX STRUCTURES IN BUOYANT AND SHEAR FLOWS

I. INTRODUCTION

The formation of ring or line pair vortices following injection of a blob of fluid into a medium at rest is a very common phenomenon. Some well-known examples include the classic "smoke ring", in which a blob of air is injected into a quiescent environment at some initial velocity. dimensional analog of this axisymmetric ring vortex formation occurs in the wakes behind lifting aircraft. The airstream behind the wings of the aircraft receives a downward momentum per unit length along the aircraft track equal to the aircraft lift. Since the downward velocity of the air is usually much smaller than the forward speed of the aircraft, this phenomenon can be thought of approximately as equivalent to the two dimensional motion that results when a cylindrical column of air is given an initial downward velocity. This motion is often observed to result in two well-defined line vortices trailing behind the aircraft wing tips.

When a spherical volume of air in the atmosphere is heated at constant pressure as a result of a point release of energy (explosion), the hot bubble of gas rises and is typically observed to develop into a toroidal ring vortex configuration by the time it has risen a distance of the order of its initial diameter. The two-dimensional analog of this axisymmetric motion can occasionally be observed in bent-over chimney plumes where the hot gas emanating from the chimney is stretched horizontally into a long cylinder by an ambient wind and then rises buoyantly. When the air is calm this long cylinder of hot gas can be observed to develop into two parallel line vortices as it floats upwards.

In the case of the smoke ring ejection and the aircraft wake the initial motion consists of a distributed sheet of vorticity embedded in a hydrodynamically irrotational flow. The subsequent development of the motion in an incompressible fluid (and in an ordinary compressible fluid when the velocities are small compared with the speed of sound) can be thought of as a mutual induction or interaction between the various sections of the vortex sheet. In the two-dimensional case in the absence of viscosity, vorticity is a transferable quantity and no new vorticity is created during the ensuing motion. In the case of the buoyant motions (rising bubble, bent-over chimney plume) the initial state may be approximated as an irrotational one with zero vorticity. The interaction between the gravitational pressure gradient and the density gradients provide a source of vorticity and the motion consists essentially of two processes - the creation of a vortex sheet or a vortex layer as a result of buoyancy and the subsequent mutual induction of different portions of this sheet. The latter induction phenomenon closely parallels the development in non-buoyant injection flows. In the buoyant phenomena the mechanics of the vorticity generation are essentially those that give rise to the well-known Rayleigh-Taylor instability. The motion of the vortex sheet in the ejection class of flows is closely related to the Kelvin-Helmholtz instability in shearing flows.

A related phenomenon is the Kelvin-Helmholtz instability that occurs at the interface between two fluids which are in relative motion. In this case the interface (vortex sheet) is unstable to the development of line vortices whose axes are perpendicular to the velocity difference vector. In the

case of a wake-like flow, which can be roughly considered as two parallel vortex sheets of layers of opposite sign, this instability results in the development of the well-known Kármán vortex street.

When horizontal shearing exists in a gravitational field in which the fluid is stably density stratified (density increasing upwards) both the Kelvin-Helmholtz mechanism and the Rayleigh-Taylor mechanism are operative. In the case of stable stratification, the Rayleigh-Taylor mechanism is stabilizing whereas the Kelvin-Helmholtz mechanism is destabilizing. Under these conditions, instabilities will develop when the destabilizing forces dominate over the stabilizing forces. The character of the motion depends on the value of the Richardson's number

$$Ri = \frac{g(d\rho_T/dz)}{\rho_T(du/dz)^2}$$

and instability occurs when Ri decreases below a certain value. Here $\rho_{\rm T}$ is the density for incompressible fluids or the "total" * density for compressible fluids.

This phenomenon is presently considered to be one of the major mechanisms creating turbulence in clear air at tropopause altitudes. In this case the stabilizing influence of an upwardly increasing potential temperature in the atmosphere inhibits development of the instabilities until a sufficiently high shearing motion can develop. The effect is of particular interest since, when the shear does develop to a high enough level to destabilize, there is potentially a large amount of kinetic energy which can be rapidly converted into vortex formation and subsequently into turbulent motion.

The conditions for onset of these various instabilities,

and characteristic wave numbers and growth times involved, have

*The word "total" refers to the density of a fluid element
when brought isentropically to a fixed reference pressure.

been studied extensively theoretically. Experimental observations are available in a variety of laboratory simulations and in various natural situations. In addition to the examples previously mentioned, phenomena which are associated with the unstable development of vortex structures include a wide variety of musical wind instruments in which the sound is dependent on the formation of vortex streets, the flapping of flags in a breeze, the whistling of wind through wires and trees (Aeolian tones), aerodynamically induced instabilities aft of bluff structures (of which a classic example is the destruction of the Tacoma Narrows suspension bridge in 1939), tornados, dust devils, thunderheads, atmospheric thermals, and hurricanes.

There is another class of flows which, though not always resulting in vortex formation, is quite similar in its hydrodynamics to the flows discussed above. These flows obtain in porous media where the inertia forces are negligible compared with the viscous forces. Here the mechanisms driving the motion are again either the initial vorticity or the vorticity induced as a result of buoyant or pressure gradient forces. Examples of this class of flows include the motion of a variable density incompressible fluid through a porous medium under the influence of gravity or a pressure gradient. In the case of the gravitational flows when a heavy liquid overlies a light liquid, the Rayleigh-Taylor mechanism is operative and the fluid will develop a motion to allow the heavy liquid to interpenetrate the lighter liquid in order to fall downward. This motion has an interesting analog in certain magnetized low-density plasmas. When a lowdensity plasma is placed in a strong magnetic field and is acted on either by gravity or weakly couples to a moving neutral background wind (the viscous interaction between the neutral

wind and the ionized plasma generally provides the coupling). The plasma coupling to the neutral background, however, is inhibited by the magnetic field. When the plasma conductivity perpendicular to the magnetic field varies with position, motion can develop which is described (in the limiting case of a very strong magnetic field and where the gradients parallel to the magnetic field are negligible) by equations that are essentially identical to the equations describing the motion of a variable density incompressible fluid in a porous medium acted on by gravity or pressure gradient forces. Instability can develop to allow the higher conductivity plasma to couple better with the background neutrals and allow it to interpenetrate the lower density plasma. This phenomenon is expected to be operative in the normal ionosphere as a result both of ambient electric fields and winds in the background neutral atmosphere. These neutral winds are collisionally coupled to the magnetized plasma and a dynamo action results which creates the electric fields that move the plasma. is thought that some of the irregular structure of the electron density distribution in the ionosphere (which is manifested as "spread-F") results from these instabilities (variously called the gradient drift instability, the $E \times B$ instability, or the Simon instability).

A phenomenon first observed in pumping of oil wells is known as "water tonguing" or "water coning". Here when the pressure at the drill stem inlet is made too low (i.e. by pumping too hard) water is observed to be mixed with the pumped oil. In these cases the oil is distributed through a sandy medium and the mechanics of the pumping consists of lowering the pressure at the well inlet so that the water surrounding the cil bed can, under its own high pressure, force the oil to the well inlet. G.I. Taylor studied this effect and concluded

that when a low viscosity fluid pushes a higher viscosity fluid through a porous medium the interface can become unstable at sufficiently high pressure gradients and torgues of water can snake through the oil towards the low pressure point. The equations of motion and the resultant instabilities are closely related to the mechanics of a two-density fluid in a porous medium, moving under the influence of gravity.

In this note we consider a class of flows in the special case where the flow consists of two incompressible liquids of different density separated by a sharp interface with or without shear across it. We will attempt to develop a simple numerical treatment of this restrictive case in a fashion that makes clear the similarities and differences between the various phenomena.

II. FORMULATION OF THE PROBLEM

II.1 General

The momentum equation for an incompressible fluid may be written in the form

$$\frac{d\vec{u}}{dt} = -\frac{1}{\rho} \quad 7p + \eta \nabla^2 \vec{u} + \vec{g}$$
 (1)

where \vec{u} is the velocity p the pressure and p the fluid density, η the kinematic viscosity, and \vec{g} is the acceleration due to gravity. The vorticity

$$\vec{\zeta} = \nabla \times \vec{u} \tag{2}$$

satisfies the equation obtained by taking the curl of Equation (1):

$$\frac{d\vec{\zeta}}{dt} = -\nabla \frac{1}{\rho} \times \nabla p + \eta \nabla^2 \vec{\zeta}$$
 (3)

Thus vorticity is generated as a result of buoyancy forces associated with density and pressure gradients and diffusively dissipates as a result of viscosity. Equation (3) provides a means for evaluating the vorticity of given fluid elements. The velocity at any point (\vec{r}) in the fluid may be evaluated from the kinematic identity (in two dimensions)

$$\vec{\mathbf{u}}(\vec{\mathbf{r}}) = \frac{1}{2\pi} \left\{ \begin{cases} \vec{\mathbf{r}}' & \mathbf{x} & (\vec{\mathbf{r}} - \vec{\mathbf{r}}') \\ |\mathbf{r} - \mathbf{r}'|^2 \end{cases} d\mathbf{x}' d\mathbf{y}' \right\}$$
(4)

where the integral extends over the entire rotational region of the fluid. The continuity equation for an incompressible fluid:

$$\frac{do}{dt} = \frac{\partial o}{\partial t} + \vec{u} \cdot \nabla o = 0$$
 (5)

can be used to follow the evolution of the density distribution

in time.

Instead of the Green's function form for the velocity field (Eq.4), the velocity may be expressed in terms of a stream function \overrightarrow{Y} :

$$\vec{\mathbf{u}} = \nabla \times \vec{\mathbf{y}} \tag{6}$$

defined such that $\nabla \cdot \vec{Y} = 0$ (the vanishing of $\nabla \cdot \vec{Y}$ is automatically fulfilled in two dimensional motion). The stream function satisfies a Poisson equation with the vorticity as the source function.

$$\nabla^2 \Psi = \zeta \tag{7}$$

for which the formal solution can be written

$$\Psi(\vec{r}) = -\frac{1}{2\pi} \int \zeta(\vec{r}') \ln |\vec{r} - \vec{r}'| dx / dy'. \qquad (8)$$

The curl of this expression yields the identity in Eq. (4).

In the present analysis we will be concerned primarily with fluids where the fractional variation of the density and viscosities are small $(\frac{\Delta \rho}{\rho}, \frac{\Delta n}{\eta}, <<1)$ and we carry out calculations only to first order in these variations. In Section II.2 we consider the two dimensional motion of inviscid fluids and in Section II.3 the motion of an incompressible fluid in a porous medium, or equivalently, the motion of an incompressible fluid confined to move between two closely spaced vertical walls (Hele-Shaw cell). The case of large density differences is treated in Section II.4.

II.2 Inviscid Fluids

When the viscosity is negligible the vorticity equation (3) takes the form

$$\frac{d\vec{\zeta}}{dt} = -\nabla \frac{1}{\rho} \times \nabla p + \vec{g}$$
 (9)

and to, first order in the density difference (since $p = \rho \cdot \vec{g} + O(\frac{\Delta \rho}{c})$,

$$\frac{d\vec{\zeta}}{dt} = -\frac{\nabla \rho}{\rho} \times \vec{g} . \tag{10}$$

For two dimensional motion in the (x,y) plane the vorticity is effectively a scalar (i.e. has only a z component). Thus, for a vertical (y direction) downward gravitational acceleration g, Equation (10) becomes

$$\frac{d\zeta}{dt} = \frac{g}{\rho} \frac{\partial \rho}{\partial x} \tag{11}$$

Of particular interest is the case of two uniform immiscible fluids of slightly differing density. In this case vorticity is generated only at the interface between the two fluids, the remainder of the flow remaining irrotational. It is convenient here to integrate Equation (11) across the interface to yield an expression for the growth rate of the surface circulation density σ (circulation per unit length along the interface):

$$\frac{d\sigma}{dt} = g \frac{(^{\circ} + ^{-\circ} -)}{^{\circ}} \sin \theta$$
 (12)

where o_{+} is the density to the right of the interface and o_{-} that to the left.

The total circulation of a given (ith) fluid element

$$\dot{\Gamma}_{i} = \int_{\zeta_{i}}^{+} dx'dy' is determined by$$

$$\frac{d\vec{\Gamma}_{i}}{dt} = g(\frac{\rho_{+} - \rho_{-}}{\rho}) \Delta y_{i} \vec{n}_{z}$$
 (13)

where Δy_i is the length or height of the fluid element in the vertical direction and \vec{n}_z is the unit vector perpendicular to the plane of motion.

A convenient numerical analysis of the evolution of the fluid motion can be obtained by dividing up the interface into a number of discrete fluid elements and approximating the circulation of each element as being concentrated into a line vortex having circulation $\Gamma_{\bf i}$. The quantity $\Delta y_{\bf i}$ is then to be interpreted as the separation between adjacent vortices. The evaluation of the fluid motion then reduces to the problem of following the motion of the individual discrete vortices. The velocity of the ith vortex is a summation over contributions from all other vortices:

$$\frac{d\vec{r}_{i}}{dt} = \vec{u}_{i} = \int_{\vec{r}\neq i}^{N} \frac{\vec{r}_{i}}{2\pi} \times (\frac{\vec{r}_{i} - \vec{r}_{j}}{|\vec{r} - \vec{r}_{j}}|^{2})$$
(14)

This equation of motion plus the relation determining the circulation growth rate (Equation 13) in which Δy_i is replaced by $\frac{1}{2}(y_{i+1}-y_{i-1})$ yields a direct deterministic procedure for following the motion.

Equations (13) and (14) have been used to calculate the evolution of a number of inviscid, buoyant and shearing flows. These calculations are discussed in Section III.

II.3 Porous Medium or Viscous Flows

When the viscosity forces dominate the inertial forces Equation (1) reduces to

$$-\frac{1}{\rho} \nabla p + \eta \nabla^2 \dot{u} + \dot{g} = 0$$
 (15)

For the flow of a fluid between two parallel plates, the flow is locally Poisuelle-like and the viscous term is dominated by the curvature of the velocity profile in the direction normal to the plates:

$$\nabla^2 \vec{u} \simeq -\frac{8\vec{u}}{d^2} \tag{16}$$

where d is the plate separation and \vec{u} is the centerline velocity. Rewriting Equation (15) we have

$$\vec{u} = -\frac{d^2}{8\eta\rho} \nabla p + \frac{d^2}{8\eta} \vec{g}$$
 (17)

A similar relation holds for flow in a porous medium. The zeroth order flow $(\nabla p = \nabla p_0, \rho = \rho_0, \eta = \eta_0)$ is a uniform velocity \vec{U}_0 :

$$\vec{U}_{O} = -\frac{d^2}{8\eta\rho} \nabla p_{O} + \frac{d^2}{8\eta} \vec{g}$$
 (18)

Taking the curl of Equation (17) we obtain for the vorticity

$$\zeta = \frac{d^2}{8} \left[-\nabla \left(\frac{1}{\rho \eta} \right) \times \nabla p + \nabla \left(\frac{1}{\eta} \right) \times \dot{g} \right]$$
 (19)

To first order in the density and viscosity variations $\triangledown p$ may be replaced by $\triangledown p_0$ where

$$\nabla p_{o} = -\frac{8\eta_{o}\rho_{o}}{d^{2}} \vec{U}_{o} + \rho_{o}\vec{g}$$
 (20)

In other words

$$\dot{\zeta} = -\frac{\nabla (\eta \rho)}{\eta_{o} \rho_{o}} \times \dot{U}_{o} + \frac{\nabla \rho}{\rho_{o}} \times \left(\frac{d^{2}\dot{g}}{8\eta}\right) . \tag{21}$$

where U_0 and g are in the same direction.

For two uniform fluids separated by a sharp interface, the surface circulation density

$$\sigma = \left(\frac{\mu_{+} - \mu_{-}}{\mu_{O}}\right) U_{O} + \left(\frac{\rho_{+} - \rho_{-}}{\rho_{O}}\right) \frac{d^{2}g}{8\eta}. \tag{22}$$

and the total circulation of a given (ith) fluid element is determined by

$$\Gamma_{i} = \left[\left(\frac{\mu_{+} - \mu_{-}}{\mu_{o}} \right) U_{o} + \left(\frac{\rho_{+} - \rho_{-}}{\rho_{o}} \right) \frac{d^{2}g}{8\eta} \right] \Delta y_{i}$$
 (23)

II.4 The Case of Large Density Differences

When the density difference is not sufficiently small, such as the case of air-sea interface, to permit the Boussinesq approximation (which essentially sets the pressure gradient in the equation for the worticity equal to a constant and uniform value) a more complex procedure is required. We consider first the somewhat contradictory case of two uniform density fluids separated by a sharp interface but having negligible surface tension. We take the fluids to be initially irrotational. According to the momentum equation

$$\frac{d\vec{\zeta}}{dt} = - \nabla \frac{1}{\rho} \times \nabla p$$

vorticity will be generated only where ∇ $\frac{1}{\rho}$ is non-zero, i.e., at the interface. Also, according to the momentum equation, the pressure gradient is partly due to a hydrostatic head (as in the Boussinesq approximation) and partly due to inertial effects in the fluid (not included in the Boussinesq approximation):

$$\nabla p = \hat{p} \vec{g} - \rho \frac{d\vec{u}}{dt}$$

Thus the generation of vorticity has two sources: first, a buoyancy term due to gravity, and second, an equivalent buoyancy term due to the fluid acceleration (an "effective" gravity):

$$\frac{d\vec{\zeta}}{dt} = - \rho \nabla \frac{1}{\rho} \times \vec{g} + \rho \nabla \frac{1}{\rho} \times \frac{d\vec{u}}{dt} = \nabla \ln \rho \times \left[\vec{g} - \frac{d\vec{u}}{dt} \right].$$

Substituting the Green's function form for expressing the velocity in terms of the vorticity field

$$\dot{\vec{u}}(\dot{\vec{r}}) = \frac{1}{2\pi} \int_{\zeta}^{+} (\dot{\vec{r}}') \times \frac{(\dot{\vec{r}} - \dot{\vec{r}}')}{|\dot{\vec{r}} - \dot{\vec{r}}'|^2} dx'dy'$$

will yield an integro-differential equation for the vorticity.

We integrate the above equation over a fixed mass element of length Δs at the surface (Figure $\stackrel{/}{\Delta}$)

$$\frac{1}{\Delta s} \frac{d\Gamma}{dt} = \frac{1}{\Delta s} \left(\frac{d\sigma \Delta s}{dt} \right) = \left(\ln \frac{\rho_2}{\rho_1} \right) \left(\frac{\dot{g}}{g} - \frac{d\dot{u}}{dt} \right)$$

where the subscript (\parallel) implies that the component parallel to the local surface inclination is desired.

Lagrangian Finite Difference Model

An implicit relation for the rates of change of the mass element circulations may be written for the model in which the interface is replaced by a number of discrete vortices.

We denote by \vec{k}_i a unit vector tangent to the surface at the point \vec{r}_i . The last equation becomes

$$\frac{1}{\Delta s_{i}} \frac{d\Gamma_{i}}{dt} = \left(\ln \frac{\rho_{2}}{\rho_{1}} \right) \left[\vec{g} \cdot \vec{\kappa}_{i} - \vec{\kappa}_{i} \cdot \frac{d}{dt} \sum_{j}^{r} \frac{\vec{\Gamma}_{j}}{2\pi} \times \frac{(\vec{r}_{i} - \vec{r}_{j})}{|\vec{r}_{i} - \vec{r}_{j}|^{2}} \right]$$

Explicitly

$$\frac{1}{\Delta s_{i}} \frac{d\Gamma_{i}}{dt} + \frac{\left(\ln \frac{\rho_{2}}{\rho_{1}} \right)^{\frac{1}{\kappa_{i}}}}{2\pi} \cdot \sum_{j=1}^{N} \frac{d\Gamma_{j}}{dt} \times \frac{\left(\vec{r}_{i} - \vec{r}_{j} \right)}{\left| \vec{r}_{i} - \vec{r}_{j} \right|^{2}} = \beta_{i} \ln \frac{\rho_{2}}{\rho_{1}} + \left(\ln \frac{\rho_{2}}{\rho_{1}} \right)^{\frac{1}{\kappa_{i}}} \cdot \vec{g}$$

where

$$\beta_{i} = -\frac{\vec{\kappa}_{i}}{2\pi} \cdot \sum_{j=1}^{N} \vec{r}_{j} \times (\vec{u}_{i} - \vec{u}_{j}) / |\vec{r}_{i} - \vec{r}_{j}|^{2}$$

$$+ \frac{\vec{\kappa}_{i}}{\pi} \cdot \sum_{j=1}^{N} \frac{\left[\vec{r}_{j} \times (\vec{r}_{i} - \vec{r}_{j})\right] \left[(\vec{r}_{i} - \vec{r}_{j}) \cdot (\vec{u}_{i} - \vec{u}_{j})\right]}{|\vec{r}_{i} - \vec{r}_{j}|^{4}} .$$

This set of equations (i = 1 to N) is a set of linear equations for the unknown quantities $d\Gamma_i/dt$.

In the limit of very large density ratios $(\rho_2/\rho_1 \rightarrow \infty;$ such as for the ocean surface), the term $(\dot{g} - d\dot{u}/dt)$ must vanish.

The equations for the vorticity generation rates $(d\Gamma_i/dt) \ \ then \ \ reduce \ to \ the \ density \ ratio \ independent \ result$

$$\vec{\kappa}_{i} \cdot \sum_{\vec{d}t} \times \frac{(\vec{r}_{i} - \vec{r}_{j})}{|\vec{r}_{i} - \vec{r}_{j}|^{2}} = \beta_{i} + \vec{\kappa}_{i} \cdot \vec{g}$$

In other words, fluid at the surface slides freely over the underlying fluid layers at a rate determined simply by gravity and the local wave slope.

II.5 Vorticity Equations with Surface Tension Effects

The momentum equation has the form

$$\frac{d\vec{u}}{dt} = -\frac{1}{\rho} \nabla_p + \vec{g} + \nu \nabla^2 \vec{u} + \text{surface tension effects.}$$

In two dimensions for an incompressible fluid, the corresponding vorticity equation is

$$\frac{d\zeta}{dc} = - \nabla \frac{1}{\rho} \times \nabla p + \text{surface tension effects} + \text{viscous}$$
 diffusion.

To estimate surface tension effects, we model the surface as a layer of finite thickness

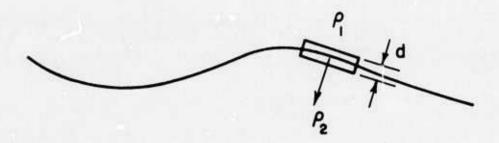


FIGURE A. A Finite Thickness Interface between Two Fluids

The net surface tension force is perpendicular to the boundary (i.e., in direction of density gradient) and is proportional to boundary curvature (K). We will model it as a body force

acting within the surface layer so that the momentum equation takes the form

$$\frac{d\vec{u}}{dt} = -\frac{1}{\rho} \nabla p + \vec{g} + \nu \nabla^{2} \vec{u} + \frac{TK}{\rho \Delta \rho} \nabla \rho$$

where T is the surface tension, K the local curvature (assumed to be uniform through the layer) and $\Delta\rho$ the density difference ($\Delta\rho$ << ρ). To transform this equation to vorticity form, we integrate along a line contour intersecting the boundary which encloses a fixed mass.

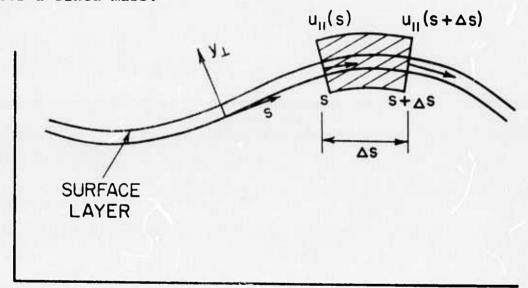


FIGURE B. Variables Defined on a Finite Thickness Interface Between Two Fluids

$$\frac{\mathrm{d}\Gamma}{\mathrm{d}t} = - \oint \frac{1}{\rho} \nabla_{\mathbf{p}} \cdot \mathrm{d}\vec{s} + v \oint \nabla^2 \vec{u} \cdot \mathrm{d}\vec{s} + \frac{\mathbf{T}}{\rho \Delta \rho} \oint \mathbf{K} \nabla_{\mathbf{p}} \cdot \mathrm{d}\vec{s} .$$

The integral over the surface tension term has contributions only from the end sections and reduces to

$$\frac{\mathbf{T}}{\rho} \frac{\partial \mathbf{K}}{\partial \mathbf{s}} \Delta \mathbf{s}$$
.

The viscous dissipation term must be treated carefully. Without the gravity and buoyancy effects the vorticity equation has the form

$$\frac{d\zeta}{dt} = v \nabla^2 \zeta$$

and implies that any concentration of vorticity will spread out by diffusion. Thus the sharpness of the interface diffuses away in time. In the present model, we wish to retain the concept of a sharp interface but at the same time to introduce an effective viscosity that will ensure smooth (or controllably smooth or rough) solutions. Thus, for numerical purposes we suppress the diffusion in the direction perpendicular to the interface. In other words, we replace the term $v \nabla^2 \zeta$ by $v \frac{\partial^2 \zeta}{\partial s^2}$ where s is the distance along the boundary. Then, integrating over our mass elements, we obtain for the viscous term

where y_{\perp} is the normal distance to the interface and σ is the surface density of circulation $(\sigma \Delta s = \Gamma)$.

The buoyancy term, in the Boussinesq approximation $(\nabla \rho/\rho <<1; \ \nabla p \ + \ -\overline{\rho}g) \ \ becomes$

$$-\frac{\Delta \rho}{\rho} g \Delta y$$

where Δy is the vertical separation of the ends of the mass element under consideration. Thus the circulation of this surface element is given by

$$\frac{d\Gamma}{dt} = -\frac{\Delta\rho}{\rho} g \Delta y + v \frac{d^2\sigma}{ds^2} \Delta s + \frac{T}{\rho} \frac{dK}{ds} \Delta s$$

In terms of the surface circulation density σ , and the surface inclination θ (radians; tan θ = dy/ds)

$$\frac{d\sigma}{dt} + \frac{\sigma}{\Delta s} \frac{d\Delta s}{dt} = -\frac{\Delta \rho}{\rho} g \sin \theta + v \frac{d^2\sigma}{ds^2} + \frac{T}{\rho} \frac{dK}{ds}$$

or

$$\frac{d\sigma}{dt} = -\sigma \frac{\partial u}{\partial s} - \frac{\Delta \rho}{\rho} g \sin \theta + \frac{d^2\sigma}{ds^2} + \frac{T}{\rho} \frac{dK}{ds} .$$

Since $\frac{d\Delta s}{dt} = \Delta s \frac{\partial u}{\partial s}$ and since on the surface*

$$\frac{d}{dt} = \frac{\partial}{\partial t} + u_{\parallel} \frac{\partial}{\partial s}$$

For finite σ there is a discontinuity across the surface in the parallel velocity. The value for u_{\parallel} in these equations is the mean $\left[u_{\parallel} = \frac{1}{2}(u_{\parallel}(+) + u_{\parallel}(-))\right]$.

we may write

$$\frac{\partial \sigma}{\partial t} = -u_{\parallel} \frac{\partial \sigma}{\partial s} - \sigma \frac{\partial u}{\partial s} - \frac{\Delta \rho}{\rho} g \sin \theta + v \frac{\partial^2 \sigma}{\partial s^2} + \frac{T}{\rho} \frac{\partial K}{\partial s}$$
$$= -\frac{\partial}{\partial s} (\sigma u_{\parallel}) - \frac{\Delta \rho}{\rho} g \sin \theta + v \frac{\partial^2 \sigma}{\partial s^2} + \frac{T}{\rho} \frac{\partial K}{\partial s} .$$

Previously we have followed specific mass elements in their motion (Lagrangian formulation). It is also convenient to divide the surface into fixed length arc segments (mixed Eulerian-Lagrangian). Let $s_{o}(s)$ be the original arc-length of the mass element which is now at the arc-length s measured from a stagnation point (i.e., a point where $u_{i} \equiv 0$ for all time). We want to develop equations for two quantities:

1) the original arc-length as a function of the present arc-length $s_{o}(s,t)$, and 2) the surface coordinates r(s,t). For the function $s_{o}(s,t)$, we note that if we write $s \neq s(s_{o},t)$, then for fixed s

$$ds = 0 = \left(\frac{\partial s}{\partial t}\right)_{t=0} dt + \left(\frac{\partial s}{\partial s}\right)_{t} ds_{0} .$$

Thus*

$$\left(\frac{\partial s_{O}}{\partial t}\right)_{S} = -\frac{(\partial s/\partial t)_{S_{O}}}{(\partial s/\partial s_{O})_{t}} = -\left(u_{\parallel}(s_{O}) - u_{\parallel}(o)\right)\left(\frac{\partial s_{O}}{\partial s}\right)_{t}$$

^{*} Subscripts identify the variable being held fixed during the partial differentiation.

where $u_{\parallel}(s_0)$ is the parallel velocity at the point $\vec{r}(s_0)$ (although $u_{\parallel}(0)$ is 0 according to our stagnation point reference, we keep the general form here). Also we may write for $\vec{r} = \vec{r}(s,t)$

$$\left(\frac{\partial \vec{r}}{\partial t}\right)_{S} = \left(\frac{\partial \vec{r}}{\partial t}\right)_{S_{O}} + \left(\frac{\partial \vec{r}}{\partial s_{O}}\right)_{t} \left(\frac{ds_{O}}{dt}\right)_{S}$$

$$= \vec{u} + \left(\frac{\partial \vec{r}}{\partial s}\right)_{t} \left(\frac{\partial s}{\partial s_{O}}\right)_{t} \left(\frac{\partial s_{O}}{\partial t}\right)_{S}$$

$$\left(\frac{\partial \vec{r}}{\partial t}\right)_{S} = \vec{u} - \left[u_{\parallel} - u_{\parallel}(o)\right] \left(\frac{\partial \vec{r}}{\partial s}\right)_{t}$$

Thus, the three equations (taking $u_{\parallel}(0) = 0$):

$$\left(\frac{\partial \vec{r}}{\partial t}\right)_{S} = \vec{u} - u_{\parallel} \left(\frac{\partial r}{\partial s}\right)_{t}$$

$$\left(\frac{\partial \sigma}{\partial t}\right)_{S} = -\frac{\partial}{\partial s} (\sigma u_{\parallel}) - \frac{\Delta \rho}{\rho} g \sin \theta + \nu \frac{\partial^{2} \sigma}{\partial s^{2}} + \frac{T}{\rho} \frac{\partial K}{\partial s}$$

$$\vec{u}(\vec{r},t) = \int \vec{\sigma} (s,t) \times \frac{\left(\vec{r} - \vec{r}'(s',t)\right)}{|\vec{r} - \vec{r}'|^{2}} ds'$$

permit following the evolution of the interface in time. In addition, the relation

$$\left(\frac{\partial s_0}{\partial t}\right)_s = -u_{\parallel} \left(\frac{\partial s_0}{\partial s}\right)_t$$

may be integrated to indicate the degree of flow movement along the boundary.

III SCALING AND LABORATORY SIMULATION

Vortex consideration furnishes a powerful ally in attacking many of the complex problems of non-linear rotational flows.

We shall, in this context, establish a working and efficient numerical basis for such approach by emphasizing the manner in which flow motion is generated by the vorticity and how the subsequent evolution develops.

In this section we study numerically models of the flows discussed in the introduction. In Section III.1, the evolution of an injection cylinder is shown to result in a pair of line vortices. In Section III.2, the buoyant rise of a cylinder of heated gas is shown to result also in the development of a line vortex pair. In Section III.3, the Kelvin-Helmholtz vortices of waves generated in a shear layer are calculated for three different Richardson numbers. In III.4, we repeat the original calculation of that of Rosenhead (1931) and that of Kronauer and Abernathy (1962) showing the development of a Karman vortex street. In Section III.5, the well known development of tip vortices is simulated. In III.6, we study a rather unique flow in which a cylinder of intermediate density fluid is placed at a stable interface between two fluids. The collapse of this cylinder as it seeks its own level results in a splitting of the original cylinder into two laterallymoving element, each of which consists essentially of a line

vortex pair. In Section III.7, a study of the same cylinder as that in III.7 is shown, but it is placed at some distance below the thermocline. In Section III.8, finally, the development of Taylor-Saffman instabilities at an interface between two viscous fluids in creeping flow is demonstrated.

III.1 Rise of an Injection Cylinder

The formation of a ring or a pair of line vortices following a sudden introduction of a blob of fluid into a quiescent medium of the same density or an impulse given to the surrounding fluid is a commonly-observed phenomenon. Examples of these are: a smoke ring, a pulsating jet, or a passage of a high-speed streamlined vehicle. In this last example, a column of ambient air will, in addition to the axial motion, be pushed into vertical ascent. The ensuing motion will be dominated by the vorticity generated as a result of the impulsive shearing motion. To simplify the problem, one could conceive a cylinder of air impulsively-injected upward so that the cylinder has a uniform velocity. If one fixes the coordinate on the cylinder, the external flow is simply a potential flow past a circular cylinder of which a solution is given as a result of a vortex doublet (Batchelor, 1967, p. 535). Since in inviscid two-dimensional and nonbuoyant flow, the vorticity is constant throughout the motion, it is convenient to attach the vorticity to the shear interface

in order to trace the boundary of the cylinder. A distribution of the vorticity along the boundary can be found to yield a uniform velocity in the cylinder. We shall return to this point after we have non-dimensionalized the governing equations.

Figure 1.la shows the initial distribution of the vortices, with the vortex axes being parallel to the generatrices of the cylinder. By symmetry, the vorticity is of the opposite signs on each half of the circle. Since there is no density difference involved in this case, the vorticity is constant throughout the motion. The motion is determined by either Equation (4) or by the set containing Equations (6) and (7). These equations are reduced to dimensionless form by introducing the following characteristic dimensions:

distance R: initial Cylinder radius

time T: $\frac{2 \mathbf{t} \mathbf{R}^2}{\Gamma_0}$

circulation Fo: total circulation assumed to be distributed on the half circle.

In terms of the dimensionless distance $\xi=\frac{\mathbf{x}}{R}$, $\eta=\frac{\mathbf{y}}{R}$, the dimensionless time $\tau=\frac{t}{T}$ and dimensionless circulation $\gamma=\frac{\Gamma}{\Gamma_0}$, then Equation (4) becomes

$$\frac{d\xi_{i}}{d\tau} = -\sum_{j\neq i} \gamma_{j} (\eta_{j} - \eta_{i}) / [(\xi_{j} - \xi_{i})^{2} + (\eta_{j} - \eta_{i})^{2}] \qquad (24)$$

$$\frac{d\eta_{i}}{d\tau} = \sum_{j \neq i} \gamma_{j} (\xi_{j} - \xi_{i}) / [(\xi_{j} - \xi_{i})^{2} + (\eta_{j} - \eta_{i})^{2}]$$
 (25)

for the Green's function formalism. In terms of the dimensionless stream function $\tilde{\Psi}=\frac{2\pi\Psi}{\Gamma_O}$ and the vorticity $\tilde{\zeta}=\frac{2\pi\zeta}{R^2\Gamma_O}$, the Equations (6) and (7) become

$$\frac{\mathrm{d}\xi_{i}}{\mathrm{d}\tau} = \frac{\partial \widetilde{\Psi}}{\partial \eta} \bigg|_{i} \tag{26}$$

$$\frac{d\eta_{i}}{d\tau} = \frac{\partial \tilde{\Psi}}{\partial \xi} \bigg|_{i} \tag{27}$$

$$\nabla^2 \widetilde{\Psi} = \widetilde{\zeta} \tag{28}$$

for the stream function formalism.

The cylinder boundary at time zero was divided uniformly into N points (61 pts. over the half circle). Each point is assumed to have a constant vorticity according to $\gamma_i = \frac{1}{2}(\eta_{i+1} - \eta_{i-1})$, i=2, N-1, and γ_1 and γ_N are equal to zero. From this distribution of discrete vortices, the velocity of each vortex can be calculated using Equations (24) and (25). To verify the uniformity of the velocity inside the cylinder, Figure 1.1b shows the initial velocity distribution. The positions of vortices are then advanced through the integration of the obtained velocities. If stream function is desirable, it can be calculated using Equation (28), and from $\tilde{\gamma}$ the velocity can be obtained for the next time step.

The vortices tend to be coagulated to the bottom center of the cylinder initially, and the purely upward translation does not take place as it occurs in the thermal which will be discussed in the next section. At $\tau=.2$, the cylinder evolves into the well-known kidney bean shape. This is shown in Figure 1.2. In Figure 1.3, the center of vorticity is well developed at $\tau=.4$ and in Figure 1.4 the vortices have rotated around the center of the vorticity several times at $\tau=1$. Batchelor (1969) showed that the centroid of the vorticety should be a constant of motion. In this study, it appears that the centroid of half of the circle $\overline{x}=\frac{2R}{\pi}$, $\overline{y}=0$ indeed remains to be constant.

We have utilized vortices of various finite core radii to obtain the velocity at each vortex from the Green's function formalism in Equations (24) and (25). When the core radius is increased, the net effect on the flow is found small on the large scale but the flow in the small scale does become smoother.

III.2 Rise of a Buoyant Cylinder (Thermal)

Scorer (1958) suggested that the behavior of plumes of smoke, when they have been bent over by a cross wind and become nearly horizontal, can conveniently be discussed in terms of a line source of buoyancy. Turner (1959) made a study of this in a water channel and observed that the plumes bent over in this way tend to split sideways into two concentrated regions with a clear space between them. He found that the flow in planes perpendicular to the axis of the plume is very like that in a vortex pair, with a region of fast rise in the center and slower regions on each side. In this section, we consider the motion of a buoyant cylinder of fluid

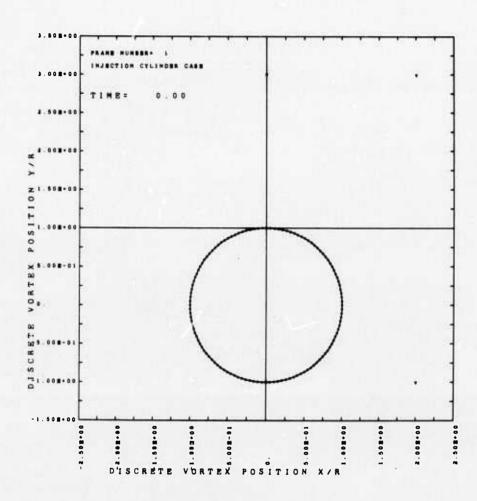


FIGURE 1.1 Initial Vortex Position of an Injection Cylinder

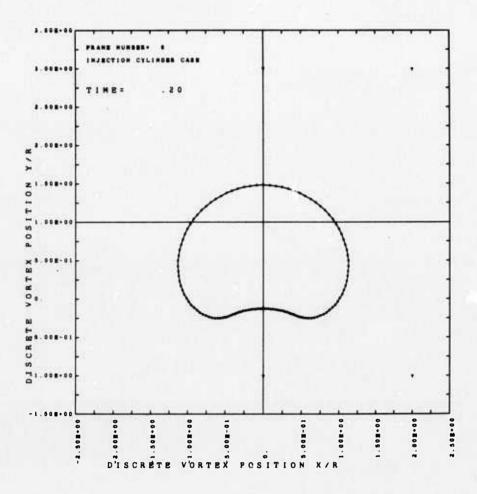


FIGURE 1.2 Injection Cylinder at $\tau = .2$

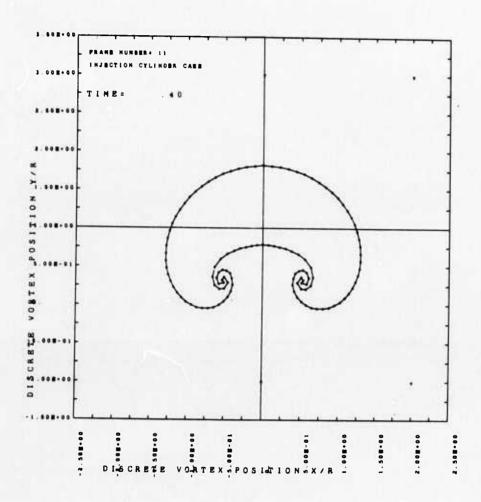


FIGURE 1.3 Injection Cylinder at $\tau = .4$

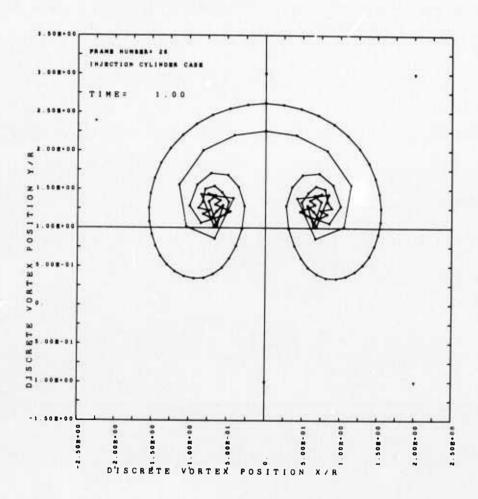


FIGURE 1.4 Vortex Pair Developed from an Injection Cylinder

floating upwards under the influence of gravity. The fluid within the cylinder is assumed initially to have a uniform density (ρ_1) and to be imbedded in a slightly more dense fluid (also of uniform density ρ_2). The fluids are assumed to be miscible (no surface tension). In this case, Equations (13) and (14) may be reduced to dimensionless form by introducing the following characteristic dimensions:

distance: R = the inital cylinder radius

time: $T = [g(\Delta \rho/\rho)/2\pi R]^{-1/2}$

circulation: $\Gamma_{o} = [2\pi g(\Delta \rho/\rho)R^{3}]^{1/2}$

In terms of the dimensionless distances, $\xi=x/R$, $\eta=y/R$, the dimensionless time $\tau=t/T$, and dimensionless circulation $\gamma=\Gamma/\Gamma_O$, the equations of motion (13) and (14) become

$$\frac{d\gamma_{i}}{d\tau} = \Delta\eta_{i} \tag{29}$$

$$\frac{d\xi_{i}}{d\tau} = -\sum_{j\neq i} \gamma_{j} (\eta_{j} - \eta_{i}) / [(\xi_{j} - \xi_{i})^{2} + (\eta_{j} - \eta_{i})^{2}]$$
 (30)

$$\frac{d\eta_{i}}{d\tau} = \sum_{j \neq i} \gamma_{j} (\xi_{j} - \xi_{i}) / [(\xi_{j} - \xi_{i})^{2} + (\eta_{j} - \eta_{i})^{2}]$$
 (31)

where

$$\Delta \eta_{i} = \frac{1}{2} (\eta_{i+1} - \eta_{i-1}).$$

Equations (29) to (31) have been used to calculate the time dependent motion in two dimensions following the release of an initially uniform circular cylinder of light weight fluid in a homogeneous heavier fluid. Since the density gradients in this example are limited to the (deforming) surface of the cylinder, the motion may be followed by following the history of the vortex sheet which comprises the cylinder boundary (see Fig. 2.1). The results of the calculation are shown in Figures 2.2 to 2.5. The cylinder boundary at time zero was divided uniformly into N points (61 points on the half circle). The velocity of each point was calculated at successive time increments according to Equations (30) and (31). The circulation of each point was calculated from Equation (29) as a function of time, the initial values being taken equal to zero (i.e., no initial motion).

The initial motion of the cylinder appears to be simply an upward displacement without sensible distortion. By the time the net displacement is of the order of 1/2 the initial cylinder radius, the beginning of vortex development is evident (Figure 2.3). The vortex appears well developed by the time the buoyant region has risen about one diameter (Figure 2.4). By this time most of the vorticity is concentrated in the vortex region. The rate of change of the total circulation of this region is obtained by summing Equation (29) over the entire vortex sheet

$$\frac{d}{d\tau} \left(\sum_{i} \gamma_{i} \right) = \delta \eta$$

or

(32)

$$\frac{d\Gamma}{dt} = g \frac{\Delta \rho}{\rho} \delta y$$

where δη is the thickness of the cap on the axis of symmetry. Thus, the value of the vortex circulation grows during the vortex development, but saturates when the vortex has fully developed. The subsequent motion (after vortex formation) of the buoyant and entrained material has been discussed by others [particularly by J. S. Turner (1959) and also by T. Fohl (1967)].

Although the present calculation was carried out for a cylindrical configuration essentially similar results are anticipated for spherical buoyant bubbles.

The entrainment process involved in this simple inviscid model thus appears to be a simple enfolding of the ambient fluid. Turbulence effects may alter the processes somewhat, particularly in determining the detailed structure and degree of mixing within the vortex core. Careful experiments are valuable for developing models that include these effects. Both experimental and numerical studies should be performed to determine the effects of large initial density differences, finite initial density gradients in the bubble, atmospheric stratification and wind shear, finite initial turbulence, and finite initial translational velocity.

At times later than 2T, when the cylinder (see Fig. 2.5) has risen more than one diameter the set of point vortices form an irregular distribution within a finite cloud. The original vortex sheet is now so convoluted as to be impossible to follow. Although the numerical model cannot be a good model of the small scale structure at such times it is interesting to note that the large scale motion agrees reasonably well with theoretical expectations (at least to values of $t \le 3T$). This may be seen as follows.

Turner (1957) has shown that the circulation of each vortex approaches a constant value after vortex formation. This may be seen from Kelvin's theorem which states that around any closed circuit C

$$\frac{d\Gamma}{dt} = \oint_{C} \frac{1}{\rho} \nabla p \cdot d\vec{s}$$

After vortex formation, the density along a path threading the center of the vortex is essentially constant and equal to the ambient value and $d\Gamma/dt \rightarrow 0$. When Γ is constant, the rise velocity varies inversely as the separation of the vortex pair

$$V \sim 1/R$$

The upward momentum increases at a constant rate

$$\frac{d(MV)}{dt} = F_B$$

where F_R is the (constant) buoyant force.

Since M is proportional to R^2 in two dimensions and RV is constant, the separation R increases linearly with time

 $R \sim t$.

Since the rise velocity of the vortex pair varies as Γ/R , the net rise distance y increases logarithmically (in two dimensions) with time

y ~ ln t

In Fig. 2.6, we show that the time dependence of the width and height of the rising vortex pair agree reasonably well with the expected dependence.

In three dimensions the expansion rate will have a different time dependence. Since here the mass varies as \mathbb{R}^3 , the momentum equation reduces to

$$\frac{dR^2}{dt}$$
 ~ constant

after torus formation (when RV ~ constant). Here R ~ $t^{1/2}$ and dz/dt ~ $t^{-1/2}$. Thus the radius of the torus increases linearly with height (R ~ z).

When the fast Fourier transform (FFT) is applied to solve the stream function, a vortex system of much larger numbers of particles can be employed costing essentially the same amount of computation time. For example, in this case,

the Green's function approach using 61 points took .246 seconds per time step. The stream function approach using 591 points took .426 seconds per step, while the same approach using 41 points costed .31 seconds per step. One drawback is, however, that the finite mode Fourier transform does produce aliasing errors. Figures 2.7 through 2.11 show the result obtained from the stream function using 200 points through the same period as that in Figures 2.1 to 2.5. The velocity vector plot seems to be smooth but the vortex position plot shows there are small fluctuations developing. If they are not eliminated, these fluctuations will be amplified into large amplitude errors. We applied a smoothing function to high wavenumber portions of the Fourier components to eliminate this noise which is well known as the Gibb's phenomenon. The result of the damping is a smoother rolled up configuration.

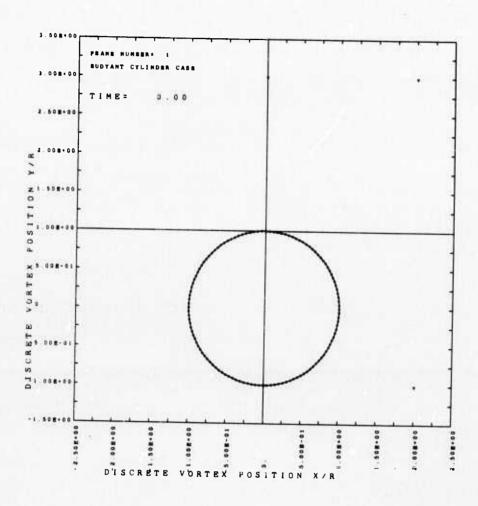


FIGURE 2.1 Initial Vortex Position of a Buoyant Cylinder

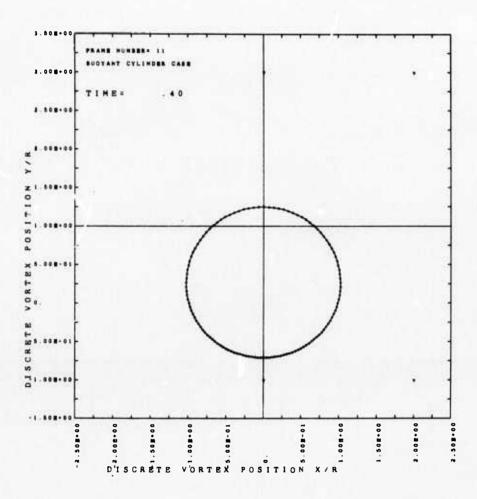


FIGURE 2.2 A Buoyant Cylinder at τ = .4

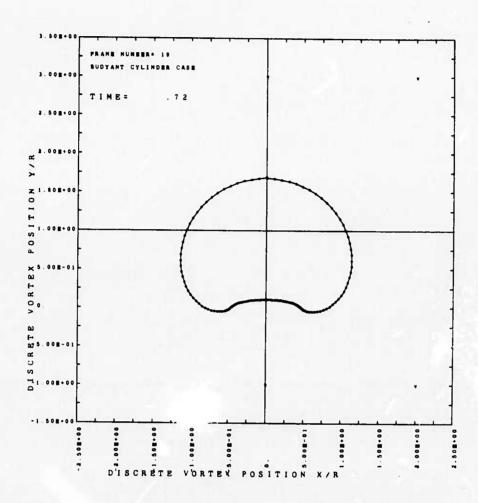


FIGURE 2.3 A Buoyant Cylinder at $\tau = .72$

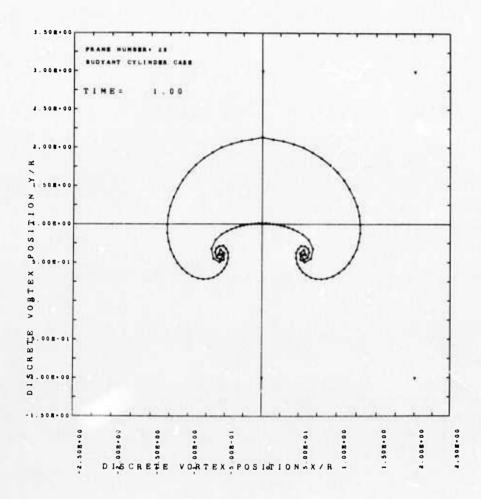


FIGURE 2.4 Vortex Pair Developed from a Buoyant Cylinder at $\tau\,=\,1$

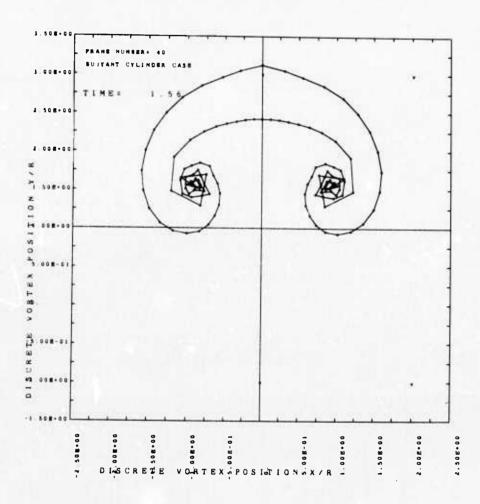
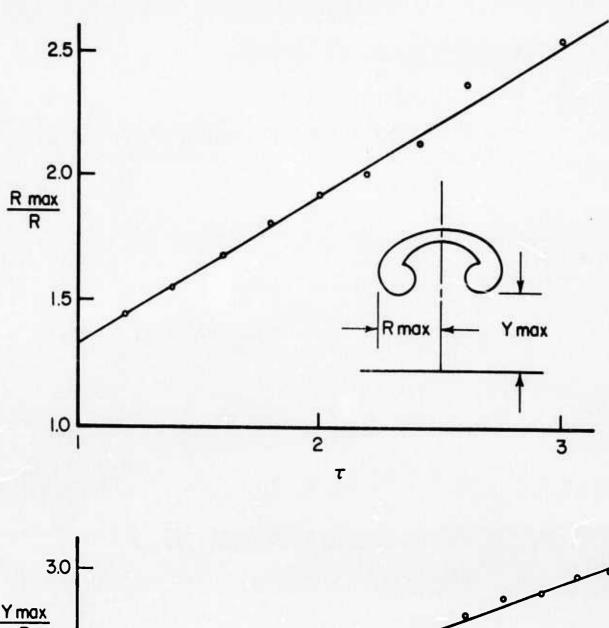


FIGURE 2.5 Vortex Pair Developed for a Buoyant Cylinder at τ = 1.56



Y max
R
2.0
0
0
0
0
1.0
4η (τ)

Fig. 2.6. The width and height of the vortex pair vs. time

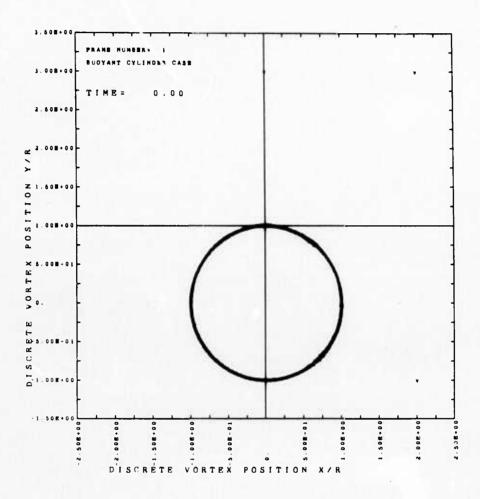


FIGURE 2.7a. Initial Vortex Position of a Buoyant Cylinder

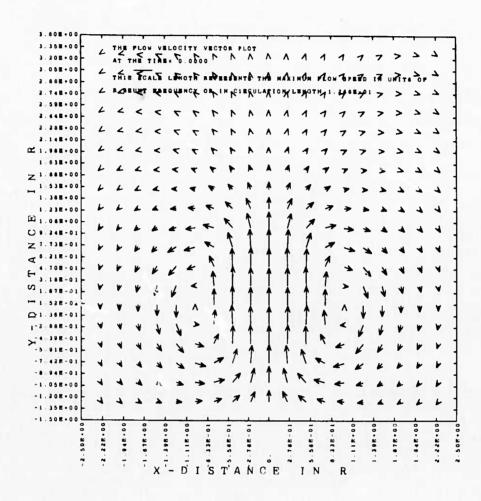


FIGURE 2.7b. Velocity Vector Plot of the Initial Vortex Position

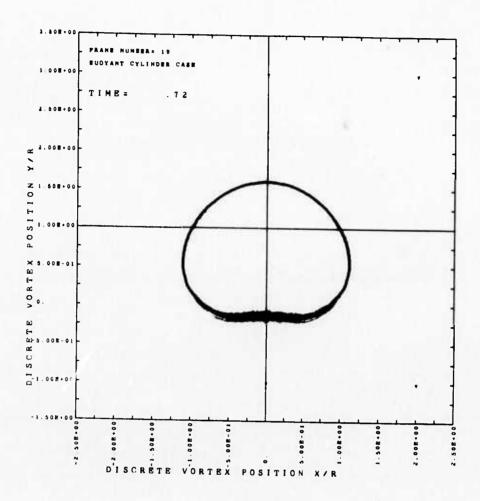


FIGURE 2.8a. A Buoyant Cylinder at τ = .72

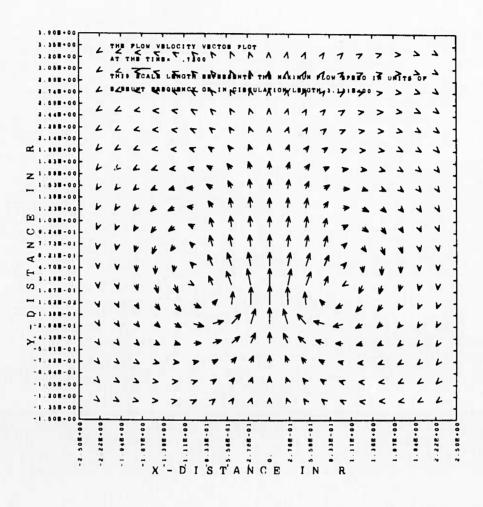


FIGURE 2.8b. Velocity Vector Plot of a Buoyant Cylinder at τ = .72

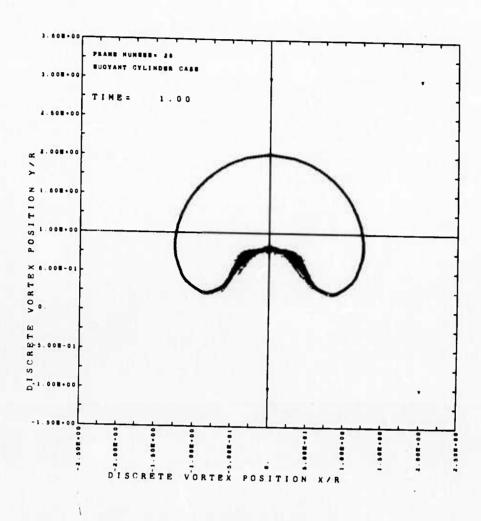


FIGURE 2.9. Vortex Pair Developed from a Buoyant Cylinder at τ = 1

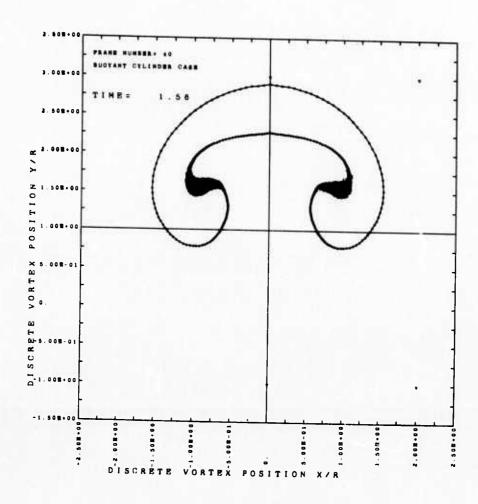


FIGURE 2.10. Vortex Pair Developed from a Buoyant Cylinder at τ = 1.56

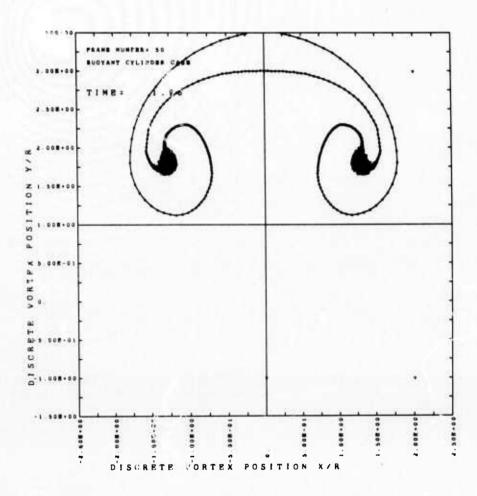


FIGURE 2.11a. Vortex Pair Developed from a Buoyant Cylinder at $\tau\,=\,1.96$

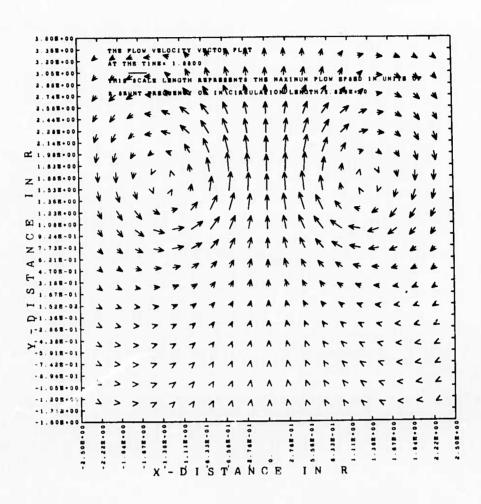


FIGURE 2.11b. Velocity Vector Plot of a Vortex Pair at $\tau = 1.96$

III.3 Finite Amplitude Kelvin-Helmholtz Waves

As early as 1868, Helmholtz found that the vortex sheet of infinite horizontal dimension formed by shear is unstable to any kind of disturbances. Recent studies of the mountain lee waves and clear air turbulence have renewed interest in studying the evolution of Kelvin-Helmholtz waves in stratified mediums. Radar backscattering studies have revealed the formation and growth of the cat's eyes in the atmosphere (Richter, 1969) and Kelvin-Helmholtz billows are also found by Wood (1969) on the seasonal themocline in the Mediterranean Sea off the coast of Malta. A numerical study of Kelvin-Helmholtz waves in a viscous fluid which solves the Navier-Stokes equations was given by Patnaik (1973).

In this section, we present the results of a study of this subject in an inviscid fluid at three effective Richardson numbers, -1, 0, 100, which are defined as R_i = $-\frac{g\Delta\rho R^3}{\rho\Gamma_O^2}$.

The equations of motion are based on Equations (24) and (25) for the case $R_i = 0$, and Equations (29), (30) and (31) for the case when $R_i \neq 0$. The infinite vortex sheet is now subjected to periodic disturbance in vertical displacement. The sum of the velocity contribution from all the vortices located at multiple wavelengths R, 2R, 3R, ... apart is evaluated by the infinite series result given by Lamb (1932). The vortex

sheet is divided uniformly into 41 points and each contains initially an equal amount of vorticity generated by the shear across it.

(i) $R_i = 0$ case (pure shear case)

The vortex sheet is given an initial disturbance shown in Figure 3.1, a sine wave of wave length R = 2, and amplitude $\frac{a}{R}$ = .1.

When the vortex sheet is rolling up, it reaches the breaking height at $\tau=.64$; that is, $t=.64\left(\frac{2\pi R^2}{\Gamma_O}\right)$ where Γ_O is the total circulation around one R length of the vortex sheet. This is shown in Figure 3.2. At $\tau=1.04$, as shown in Figure 3.3, one complete turn is made, and Figure 3.4shows the final rolled up configuration at $\tau=2$.

(ii, $R_i = -1$ (unstable) case

This corresponds to the case when the fluid is unstably stratified; therefore, large amplification of the disturbance and rapid roll up should occur. The same initial disturbance is given to the vortex sheet as in the $R_{\dot{1}}=0$ case (Fig. 3.5), except that the fluid is stratified with the lower density fluid underlying the heavier fluid. Since $R_{\dot{1}}<0$, the Brunt-Väisälä frequency becomes imaginary so that no oscillatory motion can exist. Figure 3.6 shows that the vortex sheet reaches the

breaking point at τ = .57, which is earlier than τ = .64 for the R_i = 0 case. Figure 3.7 indicates that at τ = .81, one over turn has been completed. Figure 3.8 shows that the wave has grown into a much larger roll at τ = 2 than that shown in Figure 3.4.

(iii) $R_i = 100$ (stable) case

This corresponds to the case when the atmosphere is very stably stratified, but with strong wind shear. It is an ideal situation for the generation of the internal gravity waves. One will not find any roll up, only oscillatory motion at fixed Brunt-Väisälä N = $\sqrt{-\frac{g\partial\rho}{\rho\partial z}}$. The frequency N is easily determined from the definition of the Richardson number, that is, $N = \sqrt{R_i} \, \frac{\Gamma_o}{R^2}$; hence, it is expected to take $\tau \sim 4$ to complete one cycle of oscillation.

Again, the same initial disturbance as shown in Figure 3.1 is imposed upon the vortex sheet which now possesses only ten percent of the circulation of either of the previous two cases. At τ = .99, that is at one quarter of the period of the oscillation, the vortex sheet, which is shown in Figure 3.9, becomes simply a straight line, and at τ = 2.01 (Figure 3.10), half the cycle of the oscillation is completed.

So far the calculation includes only one disturbance wavelength. For practical applications, it may be of interest to calculate interactions of disturbances with different wavelengths in

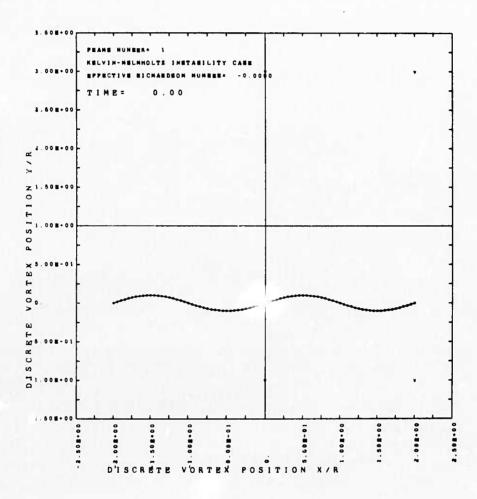


FIGURE 3.1 Initial Disturbance on a Vortex Sheet

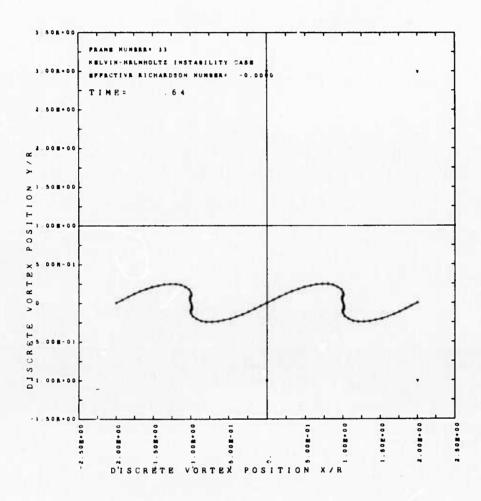


FIGURE 3.2 Kelvin-Helmholtz Wave in Pure Shear Case at τ = .64

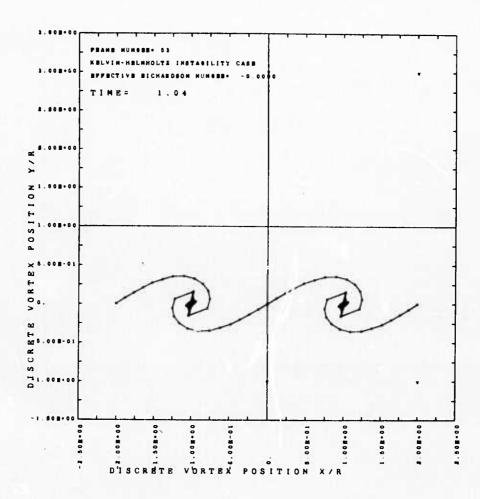


FIGURE 3.3 Kelvin-Helmholtz Wave in Pure Shear Case at $\tau = 1.04$

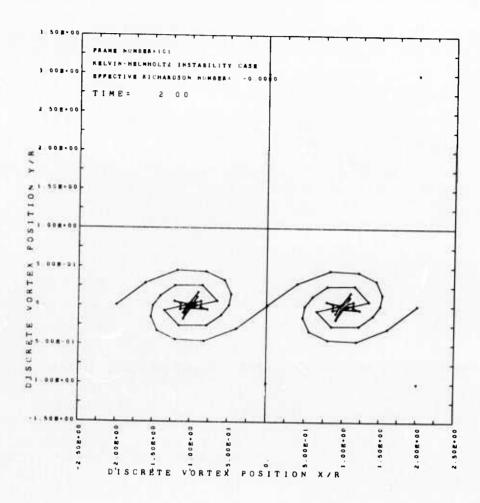


FIGURE 3.4 Kelvir-Helmholtz Wave in Pure Shear Case at τ = 2.

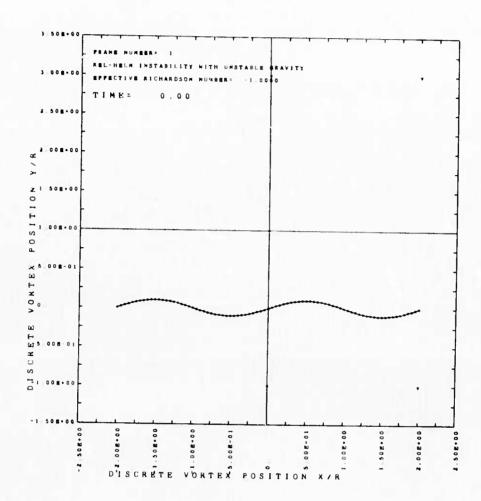


FIGURE 3.5 Initial Disturbance on a Vortex Street in an Unstably-Stratified Medium

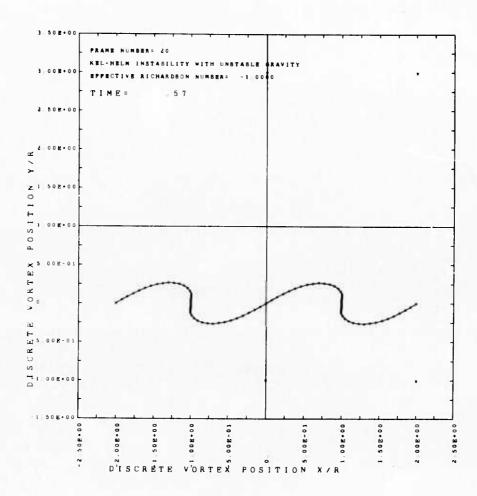


FIGURE 3.6 Kelvin-Helmholtz Wave in Unstable Case at τ = .57

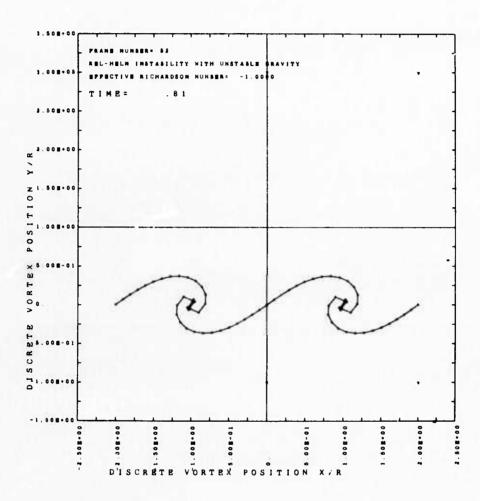


FIGURE 3.7 Kelvin-Helmholtz Wave in Unstable Case at τ = .81

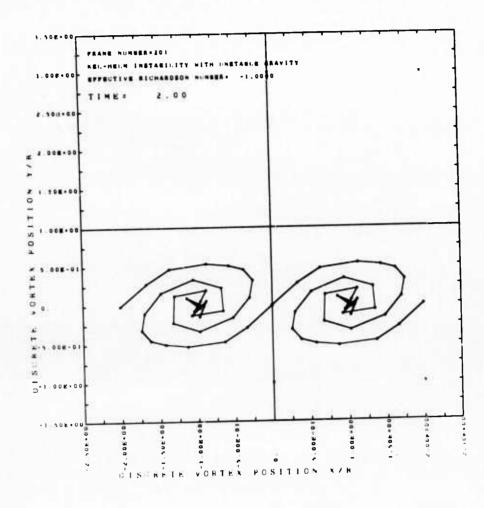


FIGURE 3.8 Kelvin-Helmholtz Wave in an Unstable Case at τ = 2

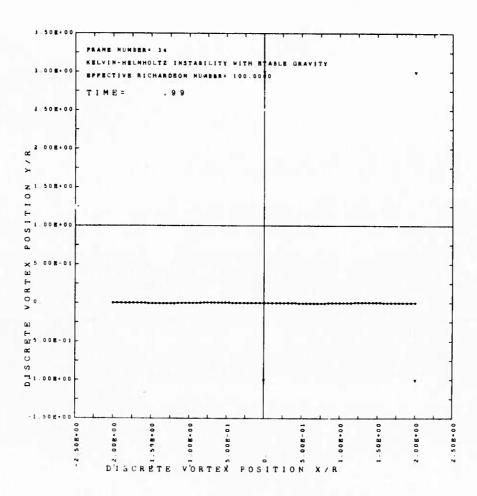


FIGURE 3.9 Kelvin-Helmholtz Wave in a Stably-Stratified Medium at τ = .99

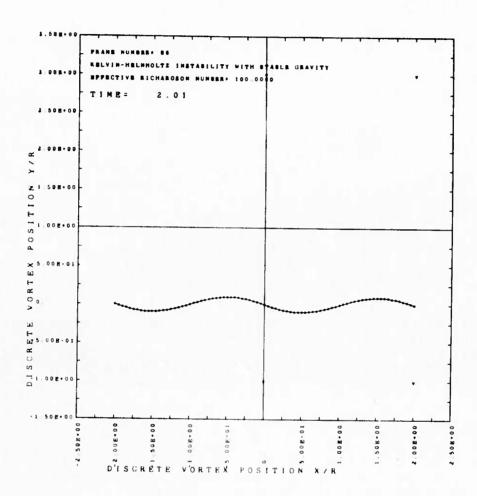


FIGURE 3.10 Kelvin-Helmholtz Wave in Stable Case at τ = 2.01

order to find the fastest growing mode. The mountain lee wave problem can also be treated conveniently through the present approach.

III.4 Development of the Kármán Vortex Street

It is well known that the vortex wake of a circular cylinder becomes unsteady once the Reynolds number based upon the cylinder diameter exceeds 40 and vortex street will develop subsequently. Kármán (1911) pointed out that when the Reynolds number increases (hence the viscosity effects decrease) the vorticity contained in each of the wake vortices will not be dissipated rapidly enough to prevent the vortex interaction among themselves. That is, for high Reynolds number flows, the study of the viscous wake can be treated as in an inviscid fluid with the motion dominated by the vortex interactions between the two vortex sheets. These sheets of opposite signs shed from the moving body in a viscous fluid can be defined as inviscid vortex sheets located at the velocity inflexion points. Since that is where it contains the most of the vorticity, the vortex sheets, once under the disturbances of different wavelengths, will evolve into different vortex street configurations. Among them, the most stable one - and therefore the most often observed one - the Karman vortex street should have a ratio of the separate distance h to the disturbance wavelength λ , $\frac{h}{\lambda}$ to be equal to .281.

The fact that the two vortex sheets are unstable to any disturbances was also predicted by the Orr-Sommerfeld stability theory which states that any velocity profile having an inflexion point is unstable, so that an unsteady analysis based upon the central theme of the vortex interactions should be carried out. The often observed unsteady separation bubble at a concave corner is a good example in this context.

Figure 4.1 shows the initial configuration of the two vortex sheets displaced vertically by a sine wave of wave length h = .28 λ ; h is the separation distance between the two sheets; the wave amplitude is $\frac{a}{R}$ = .1. The same summation given by Lamb (1932) as mentioned in Section III.3 is utilized in this section also. Figure 4.2 shows that at τ = .62, Kelvin-Helmholtz waves reach the breaking height. The dots and triangles are used to distinguish the signs of the vortex. Figure 4.3 shows that at τ = 1.2 most of the vorticity is coagulated into the alternatingly-space horseshoe vortices. Figure 4.4 shows the vortex street formed at τ = 2.10; the spacing between the vortex clouds becomes clearer and we notice that the vortices of the opposite sign are mingled. There is also a pure translation which is determined by $\frac{\Gamma_0}{R}$ toward the left.

Abernathy and Kronauer (1962) found noisy results when using vortices of zero core radius. We have obtained smoother roll up by using vortices of finite core radius. The core radius is not a critical parameter in the determination of the solution. We have conducted tests using different core radii

and found that the overall motion of the vortex system is independent of the core radius but the small scale motion loses its random character if core radius is large. Physical argument is required, however, to determine the solution at small scale. It is noted that unless a three dimensional viscous VIC method is used, the solution obtained at small scale is not meaningful. By choosing a core radius too large, the solution loses its accuracy. But by choosing too small a core radius, the solution will become noisy. Although the two dimensional VIC fails to predict the small scale motion, one can still get a fascinating glimpse into the randomization from the nearly random small scale structure within an organized large scale structure as a result of vortex interaction (as pointed out by Liepmann, 1961) and also a demonstration of the statistical characteristics of the turbulence proper. That is, the energy is transferred from large scale to small scale.

Figure 4.5 shows the initial configuration for the case when $\frac{h}{\lambda}$ = .12. Figs. 4.6 and 4.7 show the solution at τ =.92, 1.5 and Figure 4.8 shows the result at τ = 2.14. Notice that the vortices have not yet developed into the stable configuration as shown by Figure 4.4. Further coagulation will take place and will eventually lead to the Karman street.

The fact that the VIC method predicts the lateral broadering of the vortex street in the absence of viscosity and turbulence is a promising feature for the turbulence modelling by the VIC method.

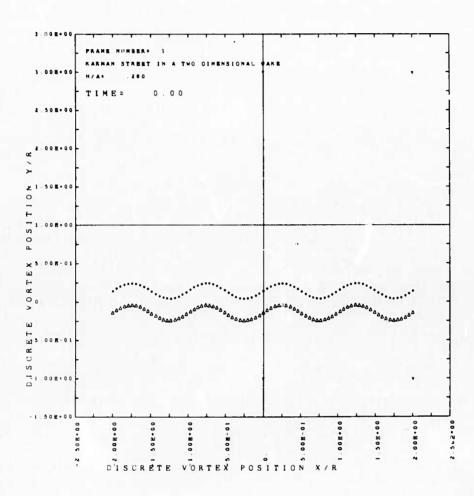


FIGURE 4.1 Initial Disturbance ($\frac{h}{\lambda}$ = .28) on a Pair of Vortex Street

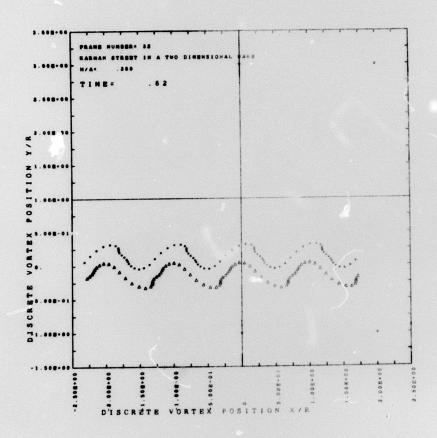


FIGURE 4.2 Development of a Vortex Street for $\frac{h}{\lambda} = .28$ at $\tau = .62$

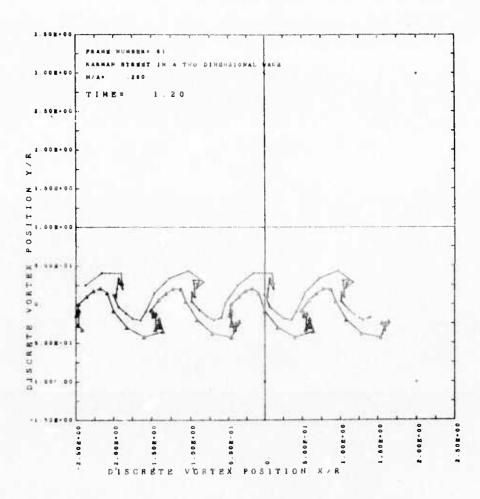


FIGURE 4.3 Development of Vortex Street for $\frac{h}{\lambda}$ = .28 at τ = 1.2

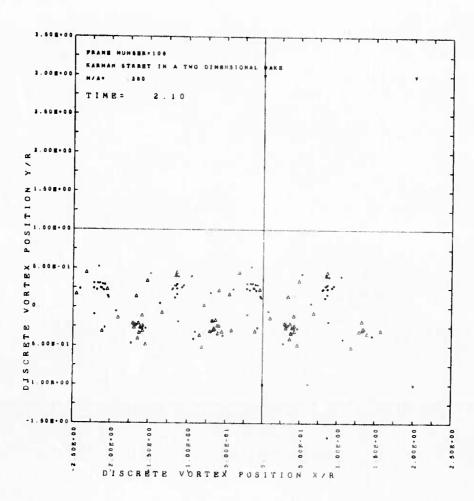


FIGURE 4.4 Distribution of Vortices in a Kármán Vortex Street

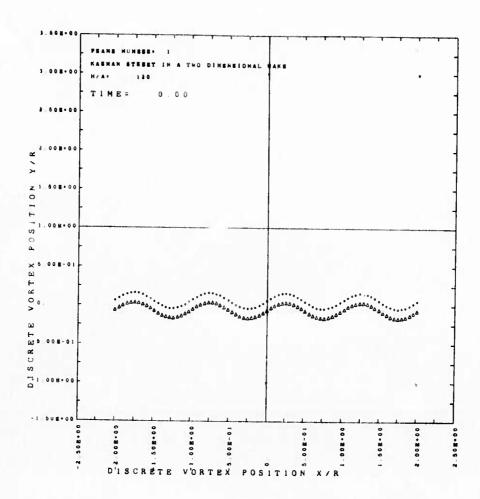


FIGURE 4.5 Initial Disturbance $\frac{h}{\lambda}$ = .12 on a Pair of Vortex Street

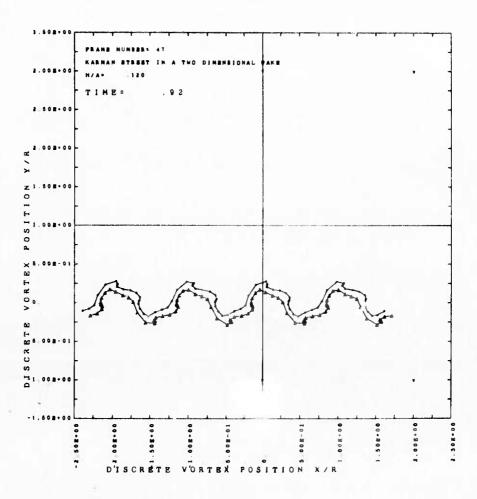


FIGURE 4.6 Development of Vortex Street for $\frac{h}{\lambda} = .12$ at $\tau = .92$

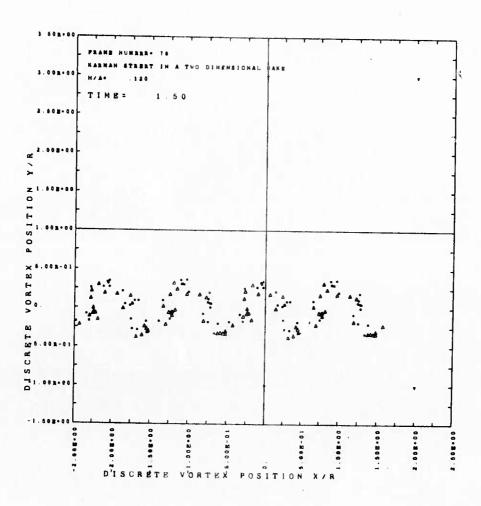


FIGURE 4.7 Development of Vortex Street for $\frac{h}{\lambda} = .12$ at $\tau = 1.5$

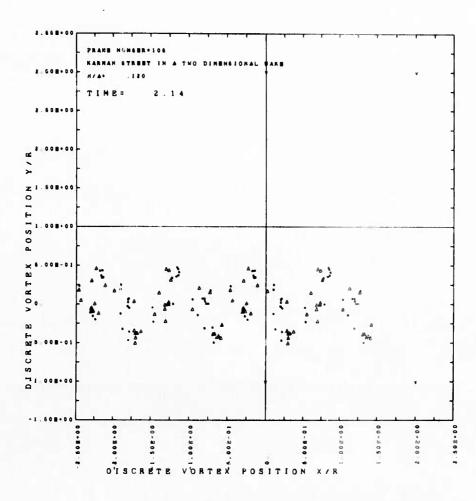


FIGURE 4.8 Development of Vortex Street for $\frac{h}{\chi}$ = .12 at τ = 2.14

III.5 Aircraft Trailing Vortex Street

By Prandtl's lifting line theory, the trailing vortex shed from the low aspect ratio wings are straight and parallel to the direction of flight and the flow in the neighborhood of any one section of the wing is approximately two dimensional and independent of the neighboring sections. This seems to be valid for most of the present day transport aircraft (excluding SST's); however, for the low aspect ratio wings, the framework laid out in this study is still applicable except that a three-dimensional formulation must be utilized. Until practical application warrants the complication, we shall assume the hypotheses in Prandtl's theory applies.

By wing theory, the lift or the wing loading is linearly proportional to the circulation about the wing cross section and it is well known that the wing load [so is the circulation S(x)] can be approximated by the elliptic curve

$$\frac{S(x)}{S_{O}} = \sqrt{1 - \left(\frac{x}{R}\right)^{2}} \tag{33}$$

where S_0 is the maximum circulation at x=0 and R is the wing span. By Stokes' law of conservation of the circulation, the circulation at

x+dx is decreased by the amount $\Delta S = S(x+dx) - S(x)$ so that this amount of circulation must be shed from the wing section between x and that at x+dx in the form of cylindrical tip vortex. Section AA' in Figure 5.1 will have a vortex sheet with variable strength resulting from the vortex shed from the wing, and the net effect of this vortex sheet is to generate a discontinuity in the horizontal velocity u along the wing surface.

Such vortex sheet is the trailing vortex commonly referred to as the aircraft wake vortex; this should not be confused with the trailing vortex shed from a twodimensional wing section due to Joukowski's analytic condition. Section BB' in Figure 1 shows this trailing vortex sheet. It is located at z = \infty and its strength has the same distribution as the wing circulation S(x) but of the opposite sign to balance the infinite tangential velocity at the trailing edge of the wing flaps. From this argument it is clear that the circulation of the trailing vortex at Section AA' is equal to the rate of change of S(x), that is $-\frac{dS(x)}{dx}$ with the proper sign. Direct differentiation of Eq. (33) with respect to the x will lead to infinity at the wing tip, hence the following relation is applied to obtain finite circulation strength at $\frac{x}{R} = 1$.

$$\frac{\Gamma(x_i)}{S_o} = \left[S(x_i) - S(x_{i+1})\right] / \Delta x \tag{34}$$

The vortex sheet is divided into NTR strips along the z direction, each segment of which contains a circulation $\Gamma_{\bf i}$ (x) given by Eq. (34).

The wind profile near the ground is known to exhibit a logarithmic dependence upon the elevation y (Blackadar and Tennekes, 1968)

$$U = \frac{u_T}{\kappa} \ln \left(\frac{Y}{Y_O} \right) + constant$$
 (35)

where u_{τ} is the friction velocity and is usually given by the relation $u_{\tau} \cong \frac{1}{30} U_{\text{at height of 1 km}}$, the κ is the Kármán constant and is equal to .42 for most applications (Hinze, 1959). The y_{0} is the roughness parameter and for typical atmospheric conditions is about .01 m.

From Eq. (35) the vertical wind shear can be obtained by taking the derivative with respect to y which yields

$$\Gamma(y) = \frac{u_{\tau}}{\kappa y} \qquad (36)$$

This circulation is assigned to each mesh point as a discrete vortex. Notice the vorticity is infinite at y = 0;

in order to avoid this we applied the following relation instead,

$$\Gamma(o) = \frac{u_{\tau}}{\kappa} \ln \left(\frac{\Delta y}{2y_{o}} \right)$$
 for $j = 1$

and

$$\Gamma(y_j) = \frac{u_{\tau}}{\kappa} \ln \left(\frac{y_j + \Delta y}{y_j - \Delta y} \right) \qquad j = 2, \dots 17 \quad (37)$$

A study of the trailing vortex shed from a Boeing 747 aircraft at a height of 61 meters (200 ft.) above the runway using a 32×32 grid was carried out. The trailing vortex was represented by 25 discrete vortices over half of the wing span, each assinged a circulation value according to Eq. (34). The wind shear vorticity is distributed over the flow domain on a 17×32 mesh, and the images are obtained by the symmetry condition in the vertical direction. The buoyant engine exhaust is also represented by 25 vortices; the temperature difference with respect to the ambient air is assumed to be 10°K. Figure 5.2a shows a Boeing 747 trailing vortex and its buoyant exhaust in a 17×32 grid.

On each grid point there is a wind shear vortex with strength determined by Eq. (37). The four downward arrows indicate the reference points of the initial geometry; all the dimensions are in kms units. Figure 5.2b shows the velocity vector plot including the trailing vortices, wind shear vortice's and their images; the maximum flow speed is represented by the length indicated on the upper left corner. From this plot, it is clear that the ground does possess some translation and the wind is blowing from the right to the left. There is a vertical downwash induced by the lift on the wing and the wind profile is significantly altered by the presence of the trailing vortices - notice the flow is opposite to the wind direction under the upwind tip vortex. Figure 5.3 shows the rolling up of the vortex sheet after 2.08 seconds, no skewness is observed at this time, and the exhaust plumes are elongated along the trailing vortices. Figure 5.4 shows the overall picture of the vortex system at t = 4.08 seconds, the wind shear vortices near the ground where the vorticity is maximum are swept up and mutual induction between those wind shear vortices and the tip vortices may be expected to emerge. Figure 5.5a shows the skewed configuration at t = 10 seconds and the exhaust plume is completely wrapped into the tip

vortices. The trailing vortices are transported nearly 40 meters to the left from the original position, and the position of the wind shear vortices delineate clearly the wind profile. Figure 5.5b shows the velocity vector plot at this time. Notice that if the vortex system is swept out of the boundary of the flow domain, the periodic condition implied by the Fourier transform will require the vortices to be replenished into the domain but at one periodic length apart from the original position. One can always choose a domain large enough to avoid the influence of the periodic images.

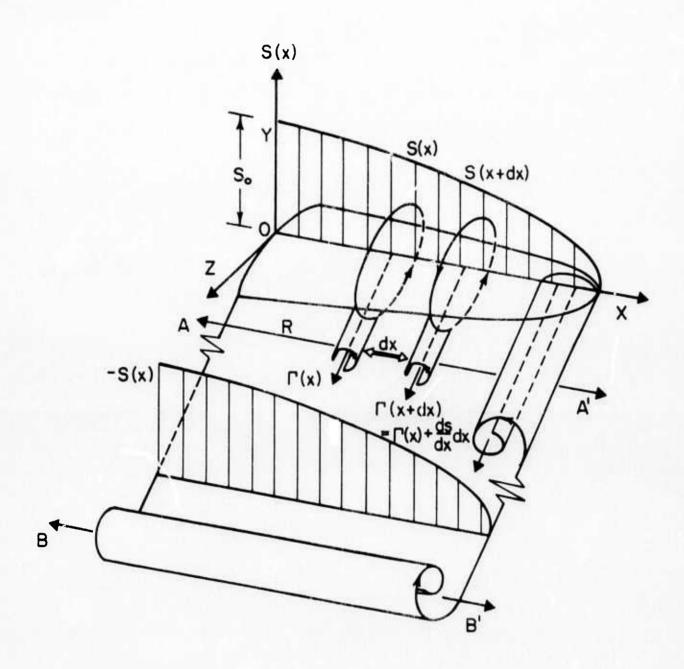


FIGURE 5.1. Determination of the strength of the aircraft trailing vortex

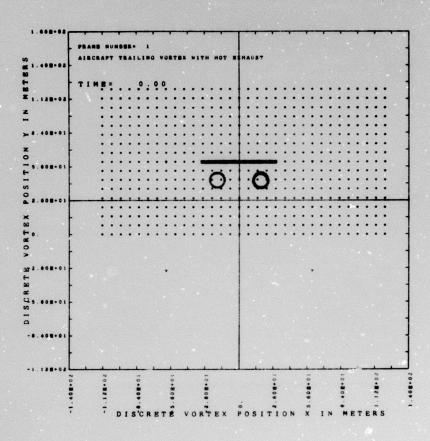


FIGURE 5.2a. Initial aircraft trailing vortex configuration

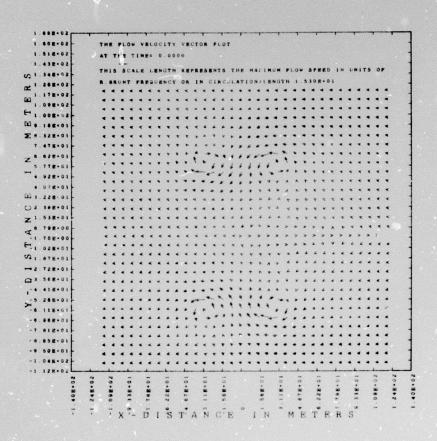


FIGURE 5.2b. Initial aircraft trailing vortex configuration

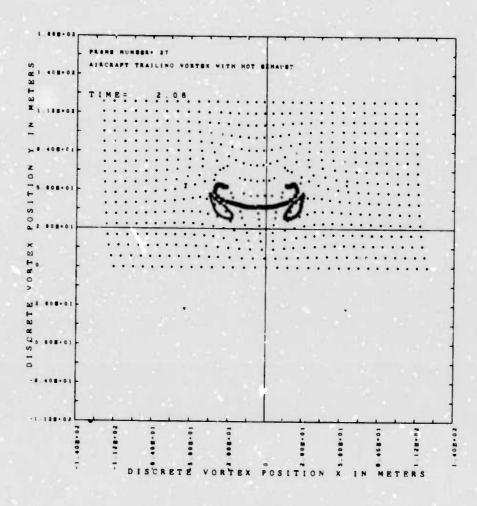


FIGURE 5.3. Aircraft trailing vortex configuration at T = 2.08 seconds

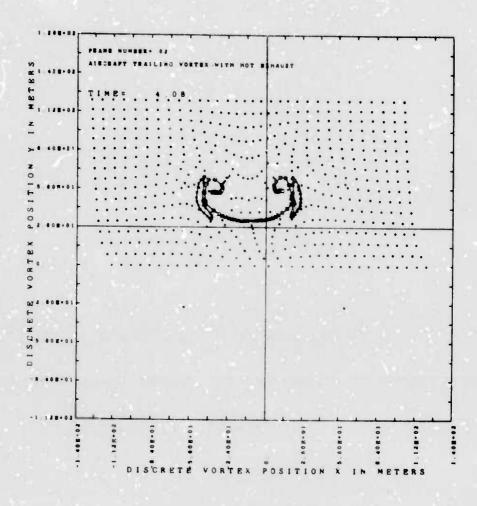


FIGURE 5.4. Aircraft trailing vortex configuration at T = 4.08 seconds

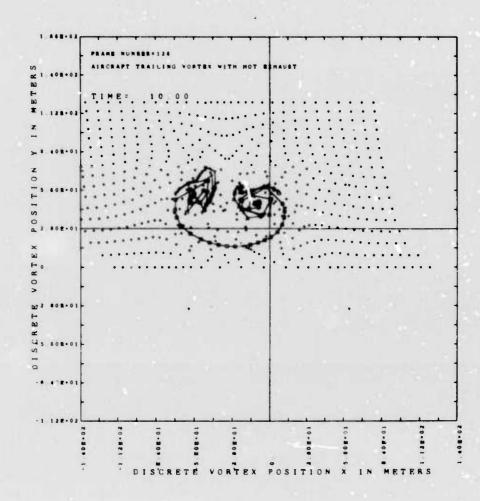


FIGURE 5.5a. Aircraft trailing vortex configuration at T = 10 seconds

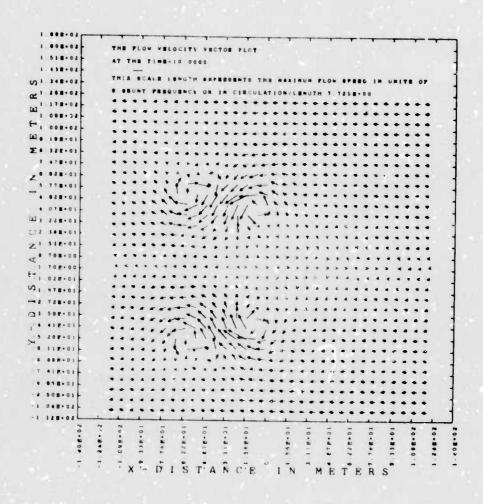


FIGURE 5.5b. Aircraft trailing vortex configuration at T = 10 seconds

III.6 Collapsing Wake on an Ocean Thermocline

We now turn to a phenomenon which is commonly treated as a hydraulic jump problem rather than from the point of view of the vortex interactions. It corresponds to the intrusion of a heavier fluid (a front or 'nose') into a fluid of lighter density. Examples of this flow are found in the atmosphere, in a weather front (say, a sea breeze), in front of a gravity current which is usually termed "Sudanese haboob", at riversea junction, at the intrusion of salt water under fresh water when a lock gate is opened, in the ocean, in a collapsing wake of intermediate density on an interface of two fluids with different densities (in other words, in an ocean thermocline) and finally in our daily lives (thin film flow on an inclined bed).

In hydraulics this is called the lock exchange problem. Many experiments have been made in this area. A summary can be found in Turner (1973). Benjamin (1968) showed that the front must have a shape of head behind which there is a turbulent region and an abrupt drop to a layer of uniform depth. Kármán (1940) showed that the shape of the nose or head at the front is 60° to the horizontal.

Figure 6.1 shows the initial geometry and its velocity vector plot. A circular cylinder of fluid of intermediate

density is formed by, for example, the propeller of a submerged vehicle on an ocean thermocline. The lines show the location of the vortices: 171 points altogether, distributed nonuniformly over the first quadrant, with the higher number density near the thermocline and fewer on the top. necessary to ensure good resolution of the nose geometry. The vorticity is initially zero. Then Equations (29) through (31) are applied to advance the calculation. Due to the lower fluid density over the cylinder and higher underneath, the buoyant force will flatten the cylinder; if there is no vorticity generated, the circular cylinder will simply be flattened into a thin layer. Due to the vorticity generated by the buoyance, there forms an advancing nose which is called the gravity current or weather front in meteorology. Notice that the maximum velocity at $\tau = 0$ is small. As it developes, Figure 6.2 shows at $\tau = .6$ the flattening wake and its velocity distribution. The velocity has grown to 1.87 in terms of the variables defined by III.2. Figure 6.3 shows the well defined nose shape at $\tau = 1.6$. The nose has a slope of nearly 60° half included angle as predicted by Karman (1940). advancing velocity is bounded by

$$\frac{1}{\sqrt{2}} \le \frac{v}{\sqrt{\frac{q \Delta \rho}{\rho} H}} \le \sqrt{2}$$

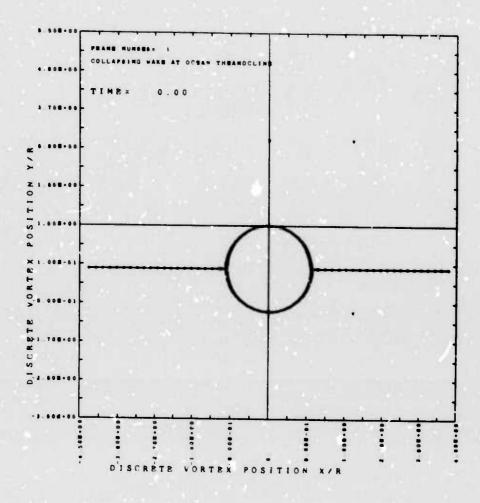


FIGURE 6.la Initial Geometry of a Cylindrical Wake at Ocean Thermocline

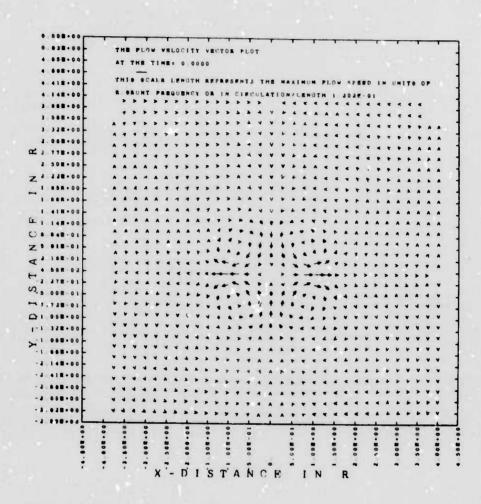


FIGURE 6.1b. Initial Geometry of a Cylindrical Wake at Ocean Thermocline

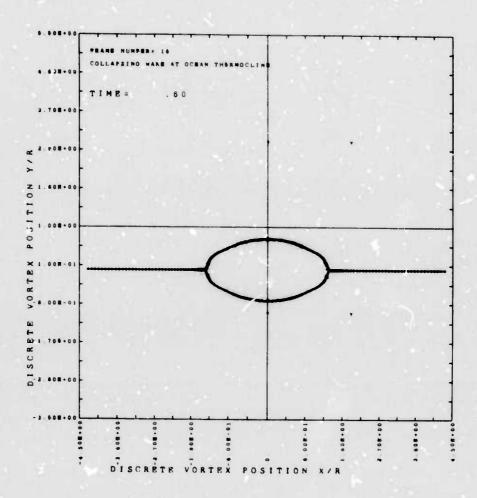


FIGURE 6.2a Collapsing Wake on an Ocean Thermocline at $\tau = .6$

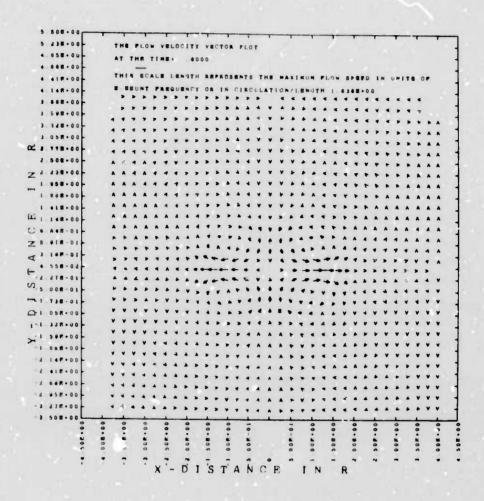


FIGURE 6.2b Collapsing Wake on an Ocean Thermocline at $\tau = .6$

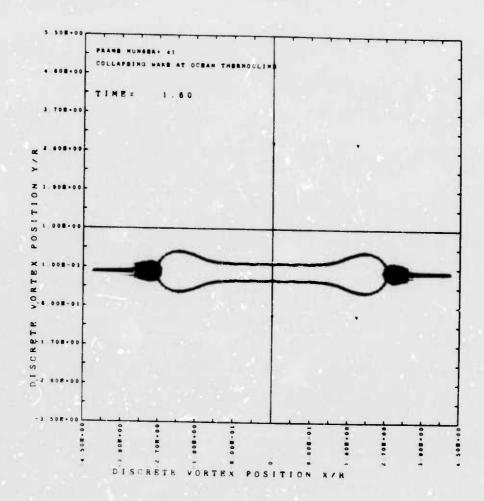


FIGURE 6.3a Collapsing Wake on an Ocean Thermocline at $\tau = 1.6$

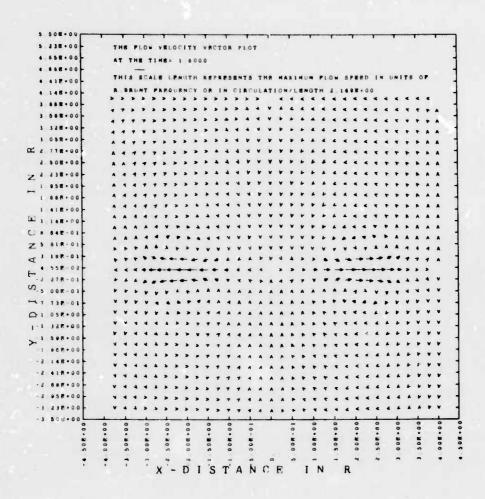


FIGURE 6.3b Collapsing Wake on an Ocean Thermocline at $\tau = 1.6$

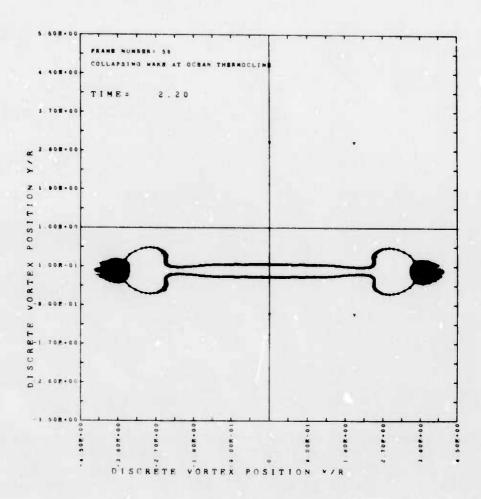


FIGURE 6.4a Collapsing Wake on Ocean Thermocline at τ = 2.2

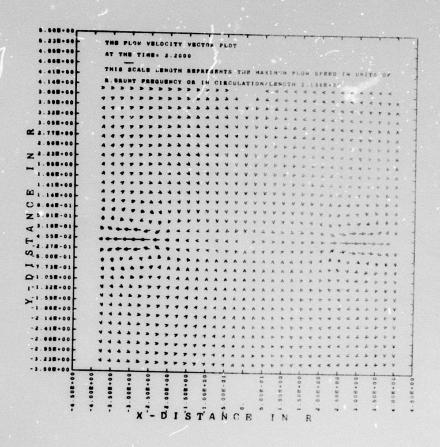


FIGURE 6.4b Collapsing Wake on Ocean Thermocline at τ = 2.2

When the ratio of the intruded layer depth H to the overlying layer depth d, H is defined by

$$\frac{1}{2} \ge \frac{H}{d} \ge 0 \quad .$$

At $\tau=1.6$, one can estimate from the above relations in terms of the presently-defined non-dimensional variables that the maximum velocity (the velocity at the nose) is approximately $2\sqrt{\pi}$, which agrees with what is shown in the velocity vector plots. At $\tau=2.2$, the solution is shown in Figure 6.4. Notice that the Kelvin-Helmholtz wave develops on the lee side of the nose. Although this is a result of the numerical noise generated by the finite mode approximation and may not exist in reality, it certainly is a simple manifestation of the instability of the flow at the shear interface. High power radar probing into the lee of weather fronts did find a braided-like structure. In this connection, we suggest it is the same result as the stationary mountain lee wave; in this case, the mountain is replaced by the moving nose.

III.7 Buoyant Wake Near an Ocean Thermocline

In this section we turn to a simple extension of the subject treated in section III.6; that is, if the wake is placed at a certain distance below a thermocline, the distance determines the upward momentum gained through the rise and

also the height that the wake overshoots its position of neutral equilibrium - the thermocline. The wake is assumed to have an intermediate density between the fluids above and below the thermocline. Due to the negative buoyance once the wake overshoots the thermocline, the wake will be flattened and unless it falls right on the thermocline, the vorticity will reverse its sign alternatingly, while spreading itself laterally. In the absence of density stratification, the wake will simply diffuse and grow both in vertical and horizontal directions. However, when the density effect dominates, the wake will be squashed and suppressed so that the residual motion consists only of large scale periodic motion; that is, the internal waves. These waves will propagate with a typical phase velocity $\sqrt{\frac{g\Delta\rho}{\rho}}$ R', where R' is the wake radius when it overshoots the thermocline. Since R' grows with t linearly, it is expected that the longer waves generated at later times will overpass the shorter waves sent out earlier. Wave breaking should occur and a finite amplitude wave front should exist as the case in III.6.

Figure 7.1 shows the initial geometry of a buoyant wake underneath a thermocline at $\frac{\mathbf{Y}}{R} = 1.2$. Notice that the maximum velocity is at the center line and is vertical upwards. At $\tau = .6$, as shown in Figure 7.2, the wake ascended through a vertical distance in the order of R = 1. A well-defined torus is formed at $\tau = 1.38$ shown in Figure 7.3.

Since it has overshot the thermocline, the negative buoyancy force is in action to flatten the top, and vorticity also becomes smaller on the top portion. One can estimate the vertical velocity at the moment using the arguments presented in Section III.2. The total vertical momentum gained through ascent (a distance $H \cong 1.5R$) is

$$\Delta (mv) = g\Delta \rho \cdot \Delta t \pi R^2$$
.

Assuming m $\stackrel{\sim}{=}$ $\rho\,R^2$ per unit length in the z-direction, and substituting $\Delta\,t\,\sim\,\frac{H}{v}$, we get

$$v \sim \sqrt{\frac{g\Delta\rho}{\rho} H}$$
.

In terms of the length R and time $\left(\frac{g\Delta\rho}{\rho}\,\frac{1}{2\pi R}\right)^{1/2}$, we get the non-dimensionalized vertical velocity

$$v = \sqrt{2\pi \frac{H}{R}} \sim 3$$

which agrees with the value appearing in Figure 7.3 velocity vector plot.

In Figure 7.4, the outgoing front bears some resemblance to that in Figure 6.3. The velocity vector plot shows that the well-defined vortex is skewed. The horizontal velocity grows at the horizontal front. One

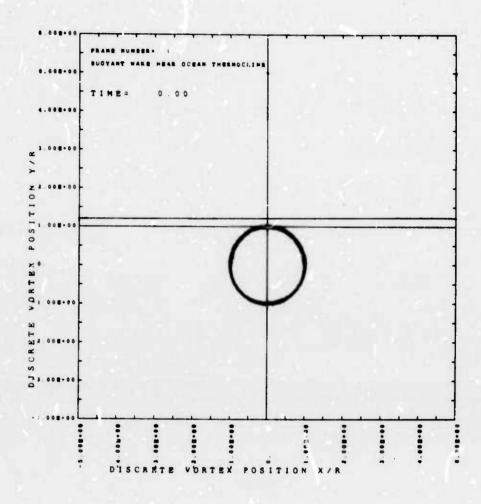


FIGURE 7.1a Buoyant Wake Near an Ocean Thermocline

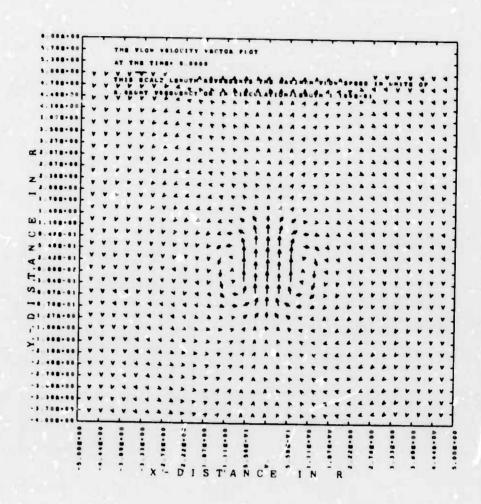


FIGURE 7.1b Buoyant Wake Near an Ocean Thermocline

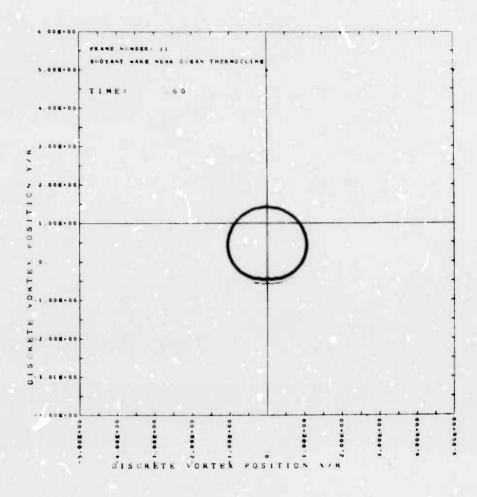


FIGURE 7.2a Buoyant Wake Near an Ocean Thermocline at $\tau = .6$

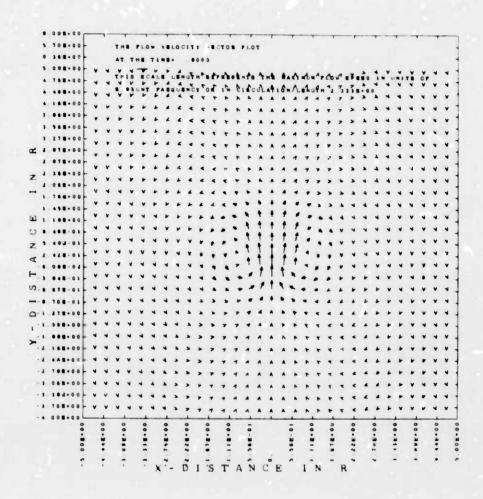


FIGURE 7.2b Buoyant Wake Near an Ocean Thermocline at $\tau = .6$

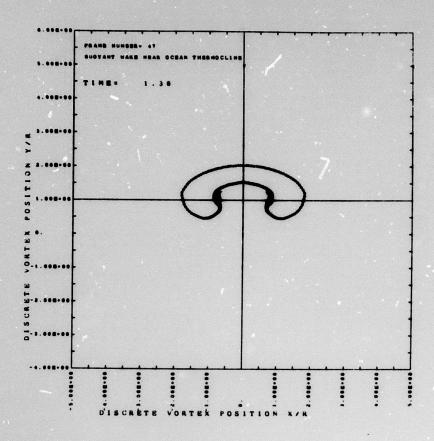


FIGURE 7.3a Buoyant Wake Near an Ocean Thermocline at τ = 1.38

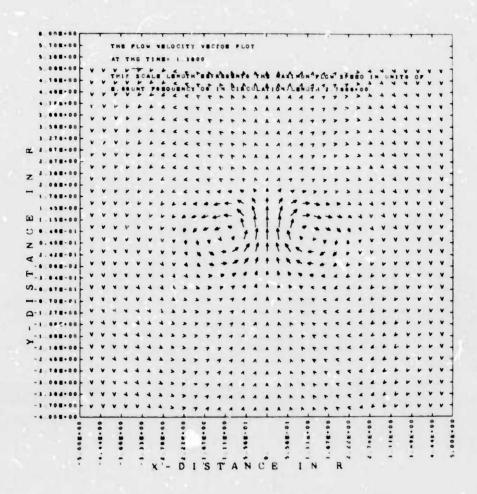


FIGURE 7.3b. Buoyant Wake Near an Ocean Thermocline at $\tau=1.38$

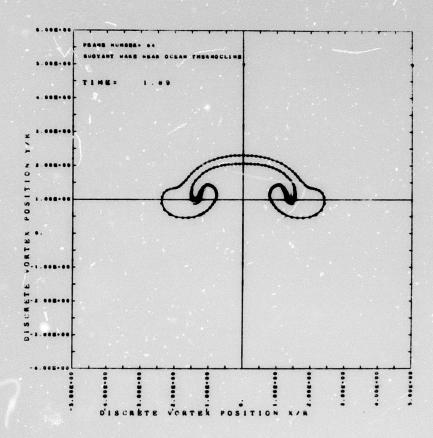


FIGURE 7.4a Buoyant Wake Near an Ocean Thermocline at τ = 1.89

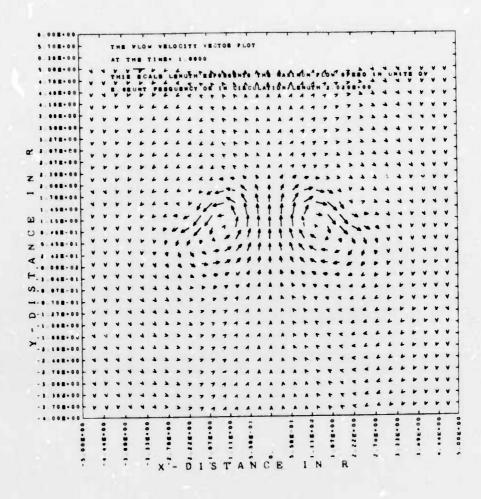


FIGURE 7.4b. Buoyant Wake Near an Ocean Thermocline at $\tau = 1.89$

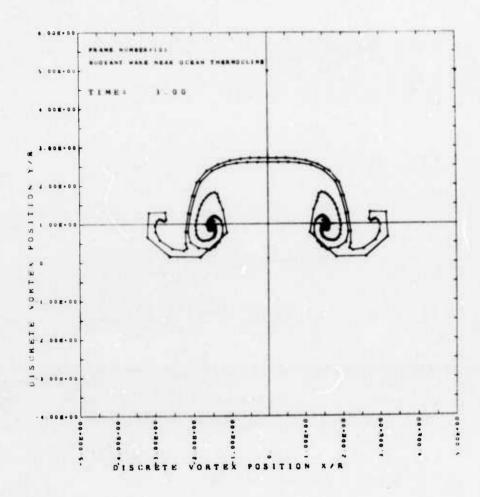


FIGURE 7.5a. Buoyant Wake Near an Ocean Thermocline at τ = 3.00

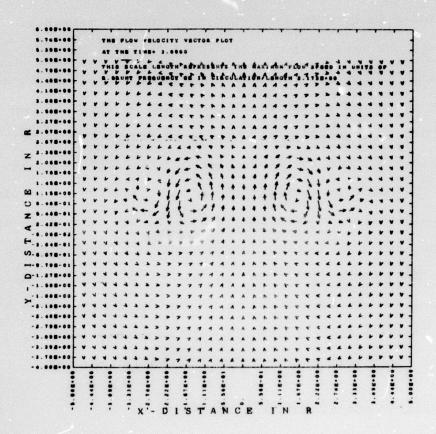


FIGURE 7.5b. Buoyant Wake Near an Ocean Thermocline at $\tau = 3.00$

cannot expect the solution in this case to evolve eventually into the one shown in Figure 6.3, because during the rise the cylinder is greatly distorted and, in the absence of viscosity, the wake will oscillate indefinitely on the thermocline at the Brunt-Väisälä frequency. The horizontal velocity at the advancing front may again be shown in the right order of magnitude, as appears in Figure III.7.4b. Figure III.7.5 shows the final plot of the calculation at $\tau=3.09$. The velocity vector plot indicates there is, in addition to the main vortex, a secondary vortex in the same sense of rotation. The solution becomes tortuous and further calculation seems unrewarding. One can always reduce the time step Δt , which was determined by the criterion that $\Delta t \sim \frac{1}{V_{\rm max}} \frac{R}{V_{\rm max}} \sim .03$. However, the calculation will be costly and only the small scale motion will be significantly improved.

III.8 Saffman-Taylor Instability

Long, narrow convecting cells, that is, the "salt fingers", are commonly observed when hot salty water is poured over cold fresh water. A very similar phenomenon occurs at the interface of two superposed viscous fluids when they are forced by gravity and an imposed pressure gradient through a porous medium. The practical examples, in addition to those already mentioned in the introduction, are oil-water interface in sand or in shale and fresh air-smoke interface in a peat moss

or a granular coal bed fire. Saffman and Taylor (1958) studied the finger-like structure in a Hele-Shaw cell and found that the ratio of the width of the finger to the spacing of the fingers is almost always equal to 1/2.

The general equation [Equation (21)] is composed of two diffusive gradients. A flow system in this context is usually called the doubly diffusive convection. One typical example is hot, salty water overlying cold, fresh water.

Equation (23) determines the circulation at the discrete vortex $(\boldsymbol{x}_1,\boldsymbol{y}_1)$. From that, the velocity field is calculated from Equation (14). To reduce these equations into dimensionless forms, we should notice that the flow is characterized by two quantities: the acceleration $\frac{g\Delta\rho}{\rho}$ and the time $\frac{k}{\eta}$, where k is the permeability and η is the kinematic viscosity. The time scale is derived as the time that it takes the viscosity to diffuse across the void area in a porous medium which is represented by k. From these two variables, we can get the following characteristic dimensions:

length R:
$$\frac{1}{2\pi} \frac{g\Delta\rho}{\rho} \left(\frac{k}{\eta}\right)^2$$

time T: $\frac{k}{\eta}$

circulation
$$\Gamma_{o} := \frac{1}{2\pi} \left(\frac{g\Delta\rho}{\rho} \right)^{2} \left(\frac{k}{\eta} \right)^{3}$$
 .

Equation (23) becomes

$$\gamma_{i} = \left(\frac{\Delta \mu}{\mu} U_{o} + 1\right) \Delta \eta_{i}$$
 (33)

where \tilde{U}_{o} is the dimensionless variable $\frac{U_{o}}{R}$ T and $\eta_{i} = \frac{Y_{i}}{R}$, $\gamma_{i} = \frac{1}{\Gamma_{o}}$. Equation (14) is reduced to Equations (24) and (25).

In order to determine the maximum allowable time step Δt , it is necessary to find the order of magnitude of the terminal velocity. We shall attempt to estimate this quantity by two means.

First, consider that the finger is replaced by a sphere of fluid accelerated under the effective gravitational force $\frac{g\Delta\rho}{\rho} \quad \text{and deccelerated by the viscous force } \mu \overline{v}^2 u \sim \mu \frac{U_{\text{terminal}}}{k}$ times the surface area of the sphere. Therefore

$$U_t \cong \frac{4}{3} \frac{g\Delta\rho}{\rho} \frac{k}{\eta}$$
.

In terms of the characteristic length and time, we have

$$\tilde{U}_{t} = \frac{8\pi}{3} .$$

Second, if we assume $U_0 \equiv 0$ for simplicity, the vorticity generated is that due to the terms $\frac{k}{\eta} \frac{\nabla \rho}{\rho_0} \times \frac{\vec{\sigma}}{\vec{\sigma}}$ only. From Figure 8.1a, the vorticity is maximum at where $\frac{\partial \rho}{\partial x}$ is the maximum. The resultant motion will be to lift up the center and push down the external edges. At some later time,

Figure 8.1b shows the growing finger where the vorticity of the opposite sign also appears, but the resultant motion is a further acceleration in the same trend as in Figure 8.1a. Assuming the final stage of the finger structure is that depicted in Figure 8.1c, we can estimate the velocity at the center top due to the vortices distributed on the now vertical interface which is of length \(\ell. \).

$$u_{t} \sim \frac{2}{\pi} \int_{0}^{\ell/2} \frac{\Gamma dy}{\sqrt{h^{2} + y^{2}}} = \frac{2k}{\eta \pi} \frac{g \Delta \rho}{\rho} \ln (y + \sqrt{h^{2} + y^{2}}) \Big|_{0}^{\frac{\ell}{2}}$$

$$- \frac{2k}{\eta \pi} \frac{g \Delta \rho}{\rho} \ln \left(\frac{\ell}{h}\right)$$

if h << $\frac{\ell}{2}$ or $\tilde{u}_t \approx 9.2$, when $\ell \approx 10h$.

From these two estimations, one can say that Δt should be approximately $\frac{1}{u_t} \cong .1$ and in fact we set $\Delta t \cong .01$ to be sure of a stable time integration.

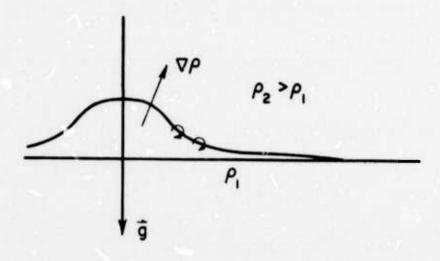
The initial disturbance corresponds to that shown in Figure 8.2. The interface is perturbed by a gaussian displacement at the center. At τ = .22, the Figure 8.3 shows that the center has risen while the edges of the gaussian displacement are depressed. Figure 8.4 shows that as the finger grows the spacing between the vortices on the top becomes large, so that unless a method by which vortices can be added to this region is implemented, one will not obtain good

resolution in this region. Notice that in Figure 8.5, at τ = .46, one vortex has been added into the center region. This repacking procedure and its aspects of economy are explained as follows.

In order to obtain reasonably good resolutions in describing the interface boundary without being committed to using a large number of vortices throughout the computation, it is essential to devise a scheme to add or deplete particles when necessary. At initial stages, the disturbance slope is small and the separation between vortices is small. Only 41 particles is enough to yield good resolution. As the fluid accelerates toward its terminal velocity (defined in a manner similar to the Stokes terminal velocity), the separation grows so that additional particles must be filled in wherever the separation is too large. The criteria to determine the repacking process is based upon the separation distance between two neighboring particles. Once a preset separation is exceeded, points are added and the circulation is redistributed among the added and the original vortices through the following procedure.

Assume that between the ith and i+lth particles, a particle is added. The new particle position is determined by a linear interpolation between ith and i+lth vortices. The circulation on the new particles is assumed to be $\frac{1}{3}$ (Γ_i + Γ_{i+1}) and the circulation on the original particles is reduced to $\frac{2}{3}$ Γ_i and $\frac{2}{3}$ Γ_{i+1} , accordingly, in order to conserve the circulation.

The sharp edges appearing in Figure 8-5 are a result of two vortices rotating around each other. Figure 8-6 shows the final result at $\tau=.98$, where the final number of vortices is N = 146. Figures 8-7 through 8-11 are the counterparts of Figures 8-2 to 8-6, but are solved by the FFT scheme, the finger structure reveals more realistic configurations than the Green's function solution.



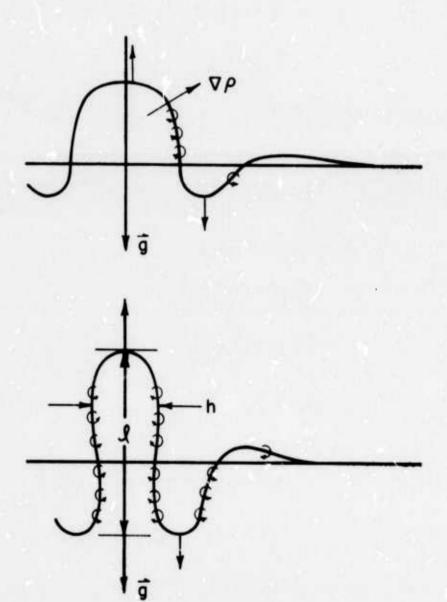


FIGURE 8.1 Development of Finger-Like Structure in Porous Medium

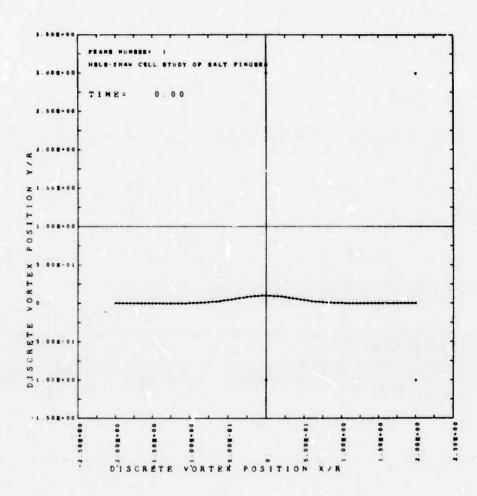


FIGURE 8.2 Initial Disturbance for the Saffman-Taylor Instability Study

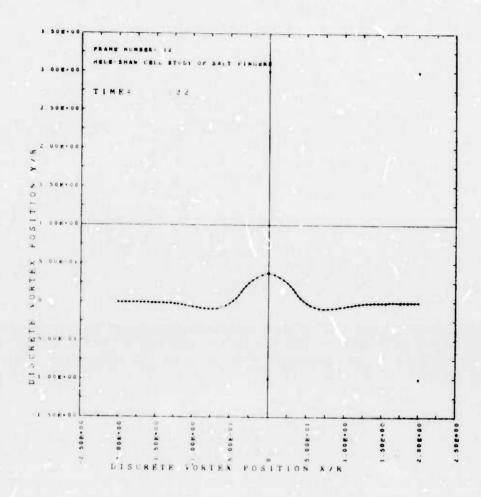


FIGURE 8.3 Saffman-Taylor Instability Study at $\tau = .22$

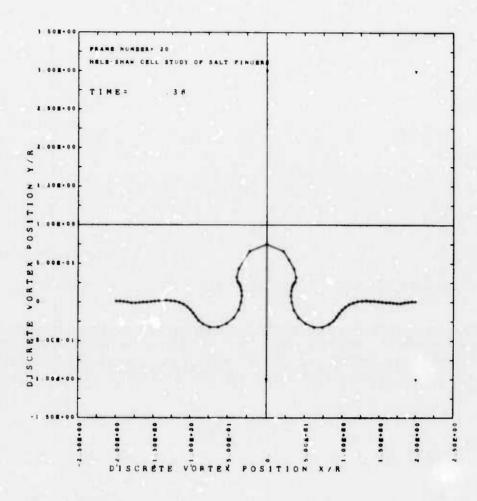


FIGURE 8.4 Saffman-Taylor Instability Study at $\tau = .38$

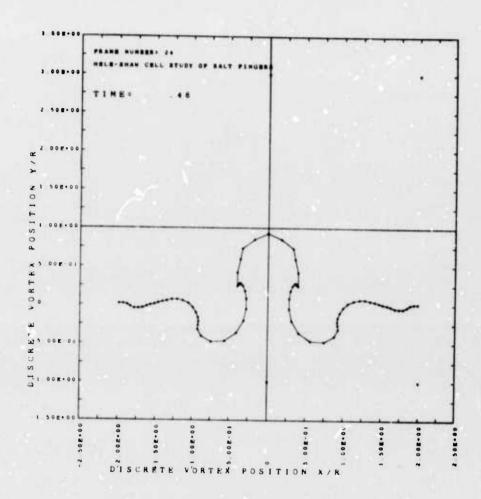


FIGURE 8.5 Saffman-Taylor Instability Study at $\tau = .46$

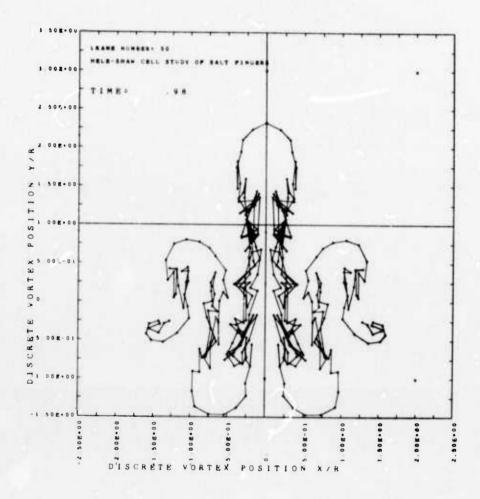


FIGURE 8.6 Saffman-Taylor Instability Study at τ = .98

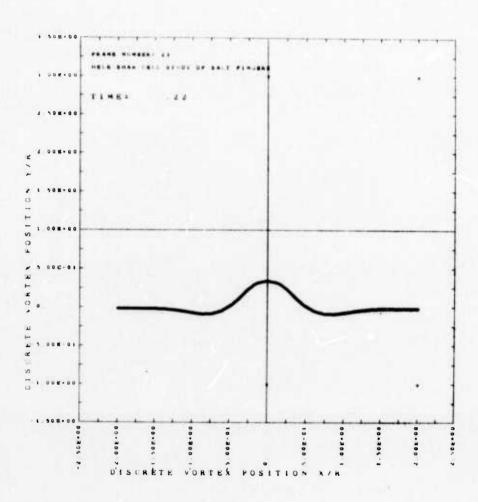


FIGURE 8.7. Saffman-Taylor Instability Study at τ = .22

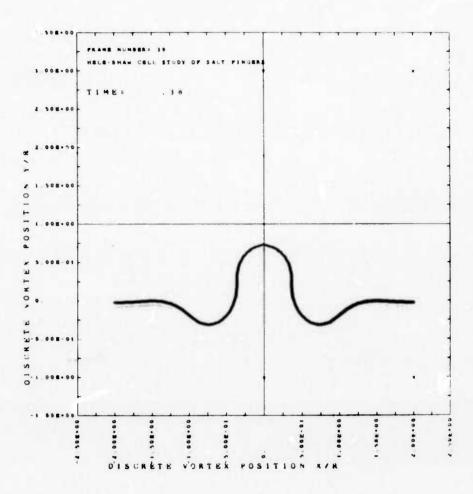


FIGURE 8.8. Saffman-Taylor Instability Study at τ = .38

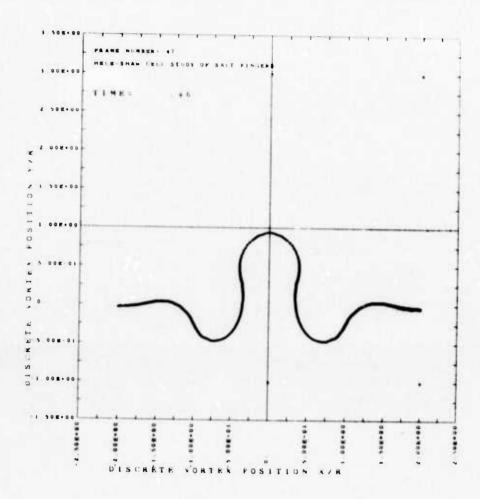


FIGURE 8.9. Saffman-Taylor Instability Study at $\tau = .46$

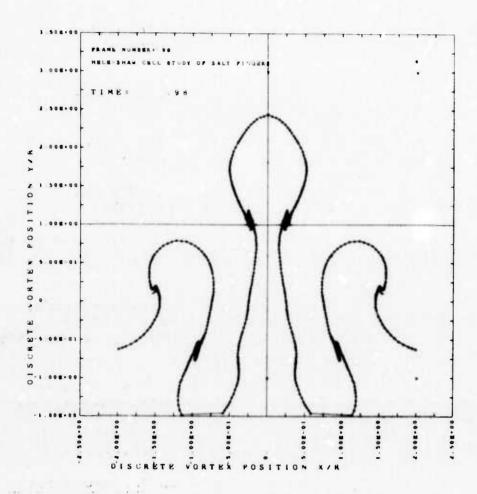


FIGURE 8.10. Saffman-Taylor Instability Study at τ = .98

REFERENCES

- Abernathy, F. H. and R. E. Kronauer, "The Formation of Vortex Streets," Journal of Fluid Mechanics 13, May-August 1962.
- Batchelor, G. K., An Introduction to Fluid Dynamics, Cambridge University Press, 1967.
- Benjamin, T. B., "Gravity Currents and Related Phenomena," J. Fluid Mech. 31, p. 2, pp. 209-248, 1968.
- Cnorin, A. J., "Numerical Study of Slightly Viscous Flow," J. Fluid Mech. 57, Part 4, pp. 785-796, 1973.
- Fohl, T., "Optimization of Flow for Forcing Stack Wastes to High Altitudes", J. Air Poll. Control Assoc. 17, pp. 730-733, 1967.
- Karman, Th. von, "Über den Mechanismus des Widerstandes, den ein kewegter Körper in einer Flussigkeit erfährt, Gottinger Nachrichten, mathematics-physics, Kl. pp. 509 -517, 1911.
- Karman, Th. von, "The Engineer Grapples with Non-linear Problems," American Mathematical Society, Bulletin 46 pp. 615-683, 1940.
- Lamb, H., Hydrodynamics, Sixth Edition, Dover, 1932.
- Liepmann, H. W., "Free Turbulent Flows" in The Mechanics of Turbulence, Gordon and Breach Science Publishers, N.Y.-London, pp. 211-227, International Symposium of the National Scientific Research Center, Marseille, August 28 to September 2, 1961.
- Patnaik, P. C., "A Numerical Study of Finite Amplitude Kelvin-Helmholtz Waves," Report No. FM-73-3, University of California, College of Engineering, November 1973.
- Richter, J. H., "High Resolution Tropospheric Radar Soundings," Radio Sci. 4, pp. 1261, 1969.
- Rosenhead, L., "The Formation of Vortices from a Surface of Discontinuity," Proc. Roy. Soc. A, 134, pp. 170-192, 1931.

- Saffman, P. G. and G. I. Taylor, "The Penetration of a Fluid into a Porous Medium or Hele-Shaw Cell Containing a More Viscous Liquid," Roy. Soc. of London, A. 245, pp. 312-329, 1958.
- Scorer, R. S., <u>Natural Aerodynamics</u>, Pergamon Press, London, 1958.
- Turner, J. S., "A Comparison between Buoyant Vortex Rings and Vortex Pairs," J. Fluid Mech. 7, Part 3, pp. 419-432, 1959.
- Turner, J. S., <u>Buoyancy Effects in Fluids</u>, Cambridge University Press, 1973.
- Woods, J. D., "On Richardson's Numbers as a Criteria for Laminar-Turbulent-Laminar Transition in the Ocean and Atmosphere," Radio Sci. 4, pp. 1289, 1969.

SHOPE SHOPE SHOPE SHOPE SHOPE SHOPE SHOPE

MISSION

Of

Rome Air Development Center

RADC is the principal AFSC organization charged with planning and executing the USAF exploratory and advanced development programs for electromagnetic intelligence techniques, reliability and compatibility techniques for electronic systems, electromagnetic transmission and reception, ground based surveillance, ground communications, information displays and information processing. This Center provides technical or management assistance in support of studies, analyses, development planning activities, acquisition, test, evaluation, modification, and operation of aerospace systems and related equipment.